universität wien

MASTERARBEIT / MASTER'S THESIS

Titel der Masterarbeit / Title of the Master's Thesis

„High pressure behaviour of α-$PbAlBO_4$ single crystals under hydrostatic compression to 24 GPa“

verfasst von / submitted by

Thomas Kremlicka, BSc

angestrebter akademischer Grad / in partial fulfilment of the requirements for the degree of

Master of Science (MSc)

Wien, 2020 / Vienna 2020

Studienkennzahl lt. Studienblatt / degree programme code as it appears on the student record sheet:	A 066 815
Studienrichtung lt. Studienblatt / degree programme as it appears on the student record sheet:	Erdwissenschaften
Betreut von / Supervisor:	Univ.-Prof. Dr. Ronald Miletich-Pawliczek

Eidesstattliche Erklärung

Ich erkläre eidesstattlich, dass ich die vorliegende Arbeit selbständig und ohne unzulässige Hilfsmittel angefertigt habe. Die verwendeten Quellen sind vollständig zitiert.

Statement under Oath

I declare on oath that I have authored this thesis independently and without undue help of any kind. All sources are fully cited.

ABSTRACT (IN ENGLISH)

In this thesis a gas loading system was used for the first time to load an ETH-type diamond anvil cell with neon for high pressure experiments under hydrostatic conditions exceeding 10 GPa. Small adaptions to the gas loading system were performed for successful operation of the system. In situ high pressure investigations of synthetic *α-PbAlBO$_4$* single crystals were performed as a test series to achieve hydrostatic compression up to 24 GPa. Third order Birch-Murnaghan equations of state were fitted to the experimentally obtained unit-cell parameters. For the unit-cell volume V_0 = 322.38(6) Å^3, K_0 = 77.5(1.2) GPa and K' = 7.3(4) and V_0 = 317.5(6) Å^3, K_0 = 109(3) GPa and K' = 5 were fitted. Changes of Raman band positions indicate the presence of two different superimposing compression mechanisms. The first mechanism is believed to be dominated by the compression of the cavity containing the Pb^{2+} cations lone electron pair, while the second mechanism is determined by the compaction of the densified structure.

ACKNOWLEDGEMENT

At this point I would like to thank Ronald Miletich-Pawliczek, who supervised this thesis, for his scientific guidance and the inviting working atmosphere he created. I also greatly appreciate the instructions, technical support and advice from Martin Ende und Erich Polacek. Last but not least I want to thank Mathias Gogolin and Thorsten Gesing (University of Bremen) for providing the sample material for this study.

TABLE OF CONTENT

1. INTRODUCTION

1.1. MOTIVATION AND OBJECTIVES

Ceramics have been around for thousands of years. While in the beginning simple clay ceramics were used, modern ceramics are often very complex. In modern context a ceramic has to be polycrystalline, synthetic, non-metallic, inorganic, consolidated at high temperatures and it may contain glass phases. Ceramics can be characterized by covalent and/or ionic bonds (Kriegesmann & Kratz, 2015). There are already existing ceramics incorporating mullite, which is not a common mineral consequently it is synthesized rather than mined. It is found in different ceramic products such as pottery, sanitary ceramics, building bricks and tiles. Due to its high temperature stability it is also used in protective coatings in high temperature environments (Anggono, 2005).

Synthetic mullite – type analogue compounds, such as *α-$PbAlBO_4$*, are therefore of interest for possible future use in ceramics. Ceramics and composites incorporating *α-$PbAlBO_4$* could be used in a variety of applications. Deep sea telecommunication systems, sensors for sonar or use in body armor (Evans and Alderson, 2000) are just a few examples to name.

Two remarkable properties of *α-$PbAlBO_4$* are the negative axial compressibility (Kalita, 2015) and the uniaxial negative thermal expansion (Gogolin et al, 2020). Especially negative axial compressibility is of interest for this thesis since there are few compounds actually showing this property. Negative axial compressibility describes the expansion of one or more dimensions during hydrostatic compression (Baughman et al, 1998). First synthesis and structural characterization of *α-$PbAlBO_4$* has been achieved by Park et al (2003). In 2015 a high pressure study has been performed by Kalita (Kalita, 2015) using synchrotron radiation on a powder sample. In this study single crystal X-ray diffractometry will be used.

The synthesis of the sample material was done by solid state synthesis using a non-stoichiometric combination of PbO, B_2O_3 and γ-Al_2O_3. The mixture was heated for 12 hours at 1073 K and then slowly cooled at a rate of 5 K/h. Crystals of *α-$PbAlBO_4$* were then removed from a glass matrix using hot diluted acetic acid (Gogolin et al, 2020).

The unit-cell parameters of the orthorhombic polymorph *α-$PbAlBO_4$* are *a=6.9209(5)Å*, *b=5.7134(4)Å*, *c=8.0215(6)Å* and Z=4. It crystallizes in *Pnma* space group. The crystal structure of *α-$PbAlBO_4$* consists of chains of [010] oriented, edge sharing AlO_6 octahedra. The AlO_6 octahedra are interconnected by alternating vertex sharing BO_3 trigonal planar groups and Pb^{2+} cations whose coordination polyhedron shares two edges with one AlO_6 chain and a vertex with another (Figure 1 & Figure 2, Park et al., 2003).

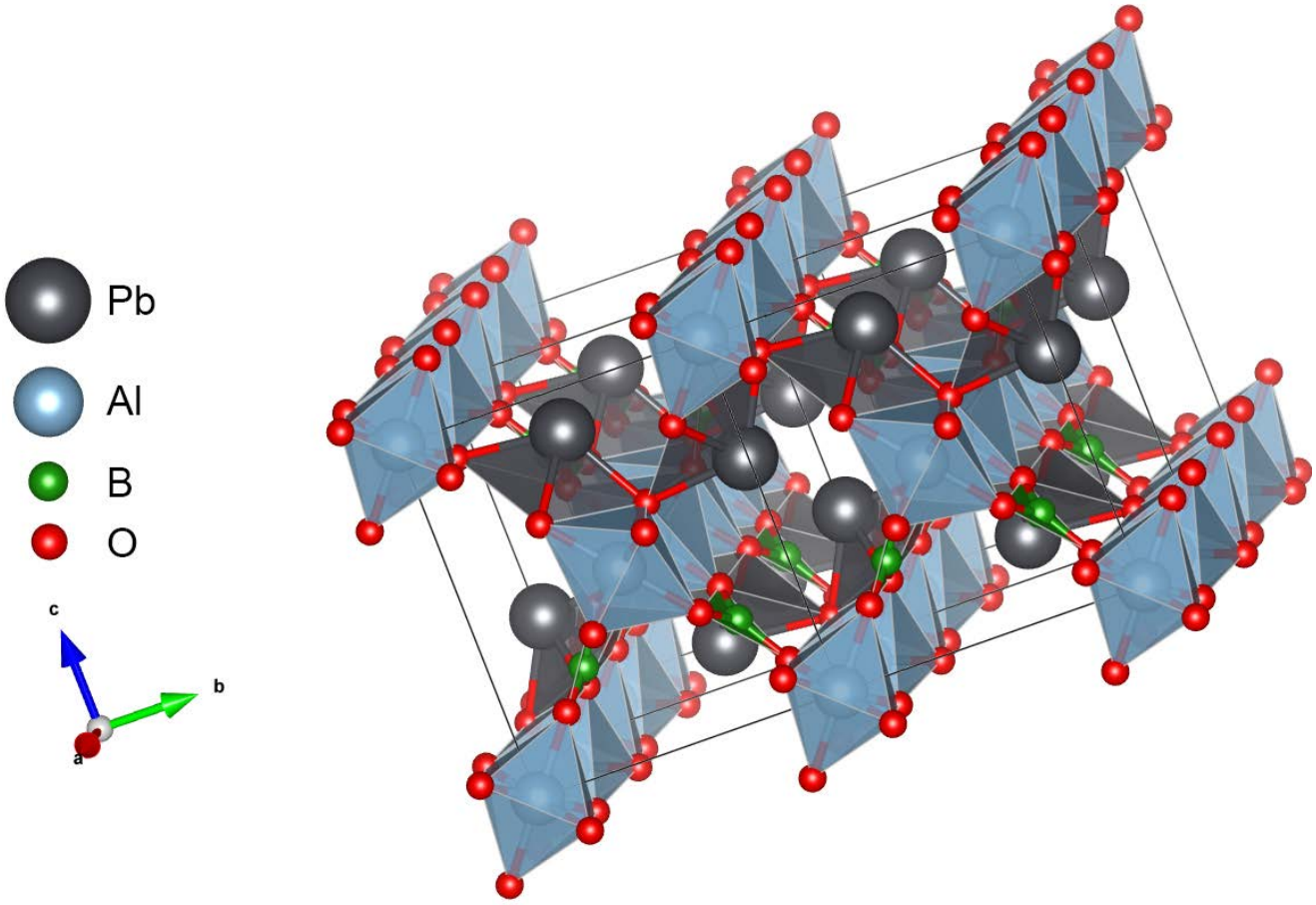

Figure 1 Crystal structure of *α-PbAlBO$_4$* presenting the chains of AlO_6 octahedra. Crystal structures are drawn using VESTA 3 (Momma & Izumi, 2011).

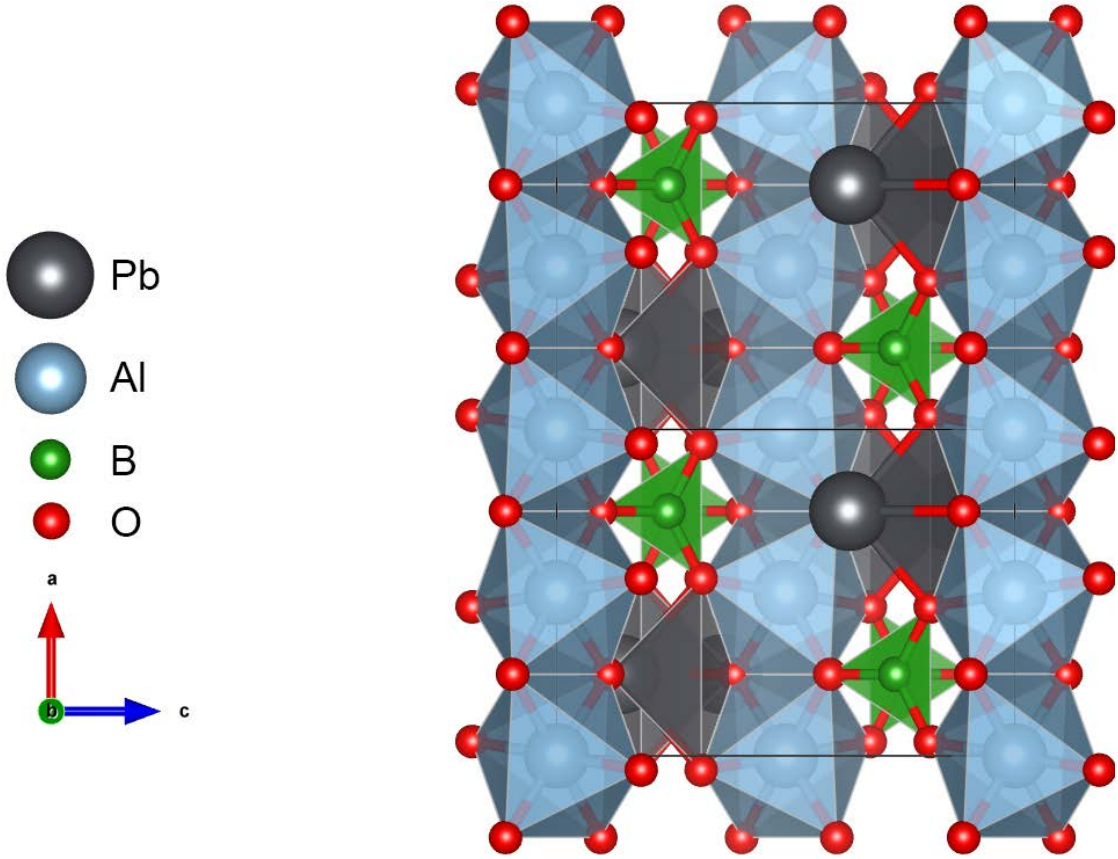

Figure 2 Crystal structure of *α-PbAlBO₄* in [010] showing the AlO_6 chains and their connections from a different perspective than in Figure 1.

The goal of this thesis is to compress a single crystal of *α-PbAlBO₄* to pressures exceeding 10 GPa to investigate its stability under isothermal hydrostatic compression. Regarding its uniaxial negative thermal expansion (Gogolin et al, 2020) a comparable structural anomaly under pressure will be evaluated. If existing in the achieved pressure range, a possible phase transition should be found. To achieve hydrostatic compression exceeding 10 GPa a reliable way to use the new gas loading system at the Institute of Mineralogy and Crystallography at the University of Vienna, which will be used for the first time, will have to be established.

2. METHODOLOGY

2.1. DIAMOND ANVIL CELL

Diamond anvil cells (DACs, Figure 3) are an important tool to investigate the behavior of materials under extreme conditions. Static pressures in the Mbar region can be achieved using DACs. For this study ETH-type DACs (Allan et al., 1996, Miletich et al, 2000) were used to perform Raman spectroscopy and X-ray diffraction under high hydrostatic pressure.

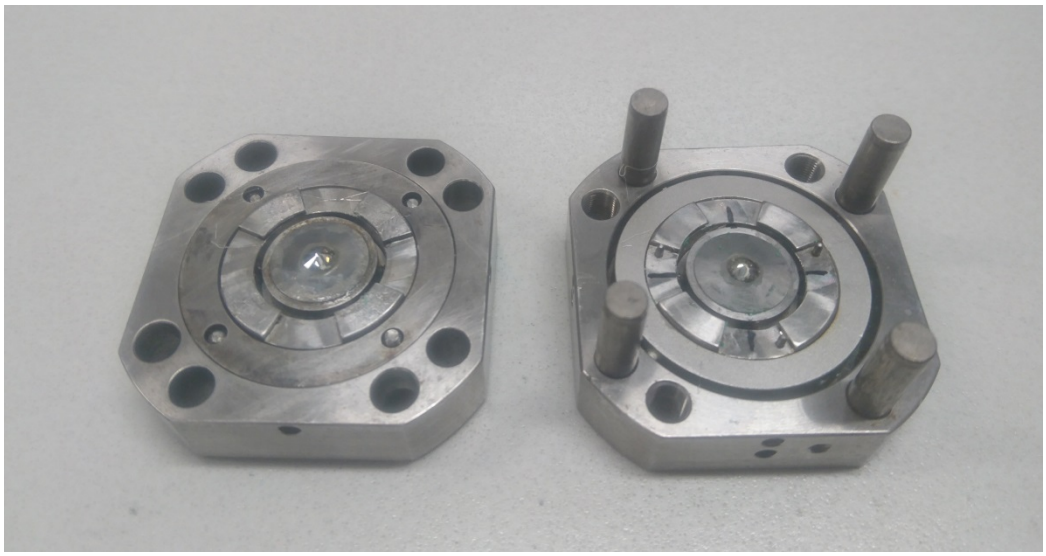

Figure 3 Two main components of the unloaded ETH-type DAC with Böhler-Almax cut diamonds.

Two types of diamond anvils, standard brilliant cut and Böhler-Almax, were used. In both cases the top of the diamonds is cut off to get a planar face (culet). While the standard brilliant cut diamonds are held in place by pressing them on a beryllium plate using a metal sheet, the Böhler-Almax diamonds are glued onto the conical interface of a tungsten carbide support.

A steel or rhenium gasket, which is placed between the culets of the two diamonds, has a hole drilled to serve as the pressure chamber.

2.1.1. LOADING

As pressure medium a mixture of 4:1 methanol:ethanol was used for experiments up to 10GPa. Steel gaskets, which are about 250 µm thick, were indented using the DAC. The imprint was about 100 µm in thickness. A hole with 250 µm diameter was then drilled into the middle of the imprint using a BETSA MH20M spark eroder.

For experiments which were expected to go above 10 GPa, neon was used as pressure medium. For these experiments the imprint into the steel gaskets was about 160 µm and the hole was 300 and 400µm in diameter. However the 400 µm was not stable enough to yield successful results. In

order to achieve pressure exceeding 10 GPa a rhenium gasket with 120 µm imprint and 250 µm hole diameter was used.

For X-ray diffraction and Raman spectroscopy experiments a single crystal of *α-$PbAlBO_4$*, a single crystal of synthetic quartz and synthetic rubies were loaded. For experiments which were only supposed for Raman spectroscopy a single crystal of *α-$PbAlBO_4$* and synthetic rubies were loaded.

A small amount of grease was used to attach the crystals to the diamond in every loading.

2.1.2. Gas Loading System (Autoclave)

To fill the pressure chamber with neon a special system was used. The first step was to insert the DAC into a kind of clamp (Figure 4). The screws of the DAC had to be open by about a three quarter rotation from being closed. To keep it open against soft pressure small pieces of styrofoam were wedged between the two halves of the DAC.

Figure 4 Clamp used to hold the DAC (left). Autoclave pressure chamber (right).

The clamp holding the DAC has to be inserted into the pressure chamber of the autoclave and the screws at the back have to be put onto the hex pins. They can be used to tighten or loosen the clamp with wheel behind the pressure chamber (Figure 4) which is also present behind the safety wall (Figure 5). Afterwards the pressure chamber is closed and filled with neon gas. Compressed neon will be pumped in until a pressure of 1400 bar is reached. Then the wheel will be turned counterclockwise for about 1 rotation to close the DAC using the clamp. To make this easier a rotation indicator on the safety wall is used (Figure 5). The pressure chamber can then be depressurized and opened. Using two allen keys the DACs screws can then be tightened while still inside the clamp. Afterwards the clamp can be removed by turning the wheel back to the starting point and pulling it from the pressure chamber. The DAC can then be taken from the clamp and is ready to be used for experiments.

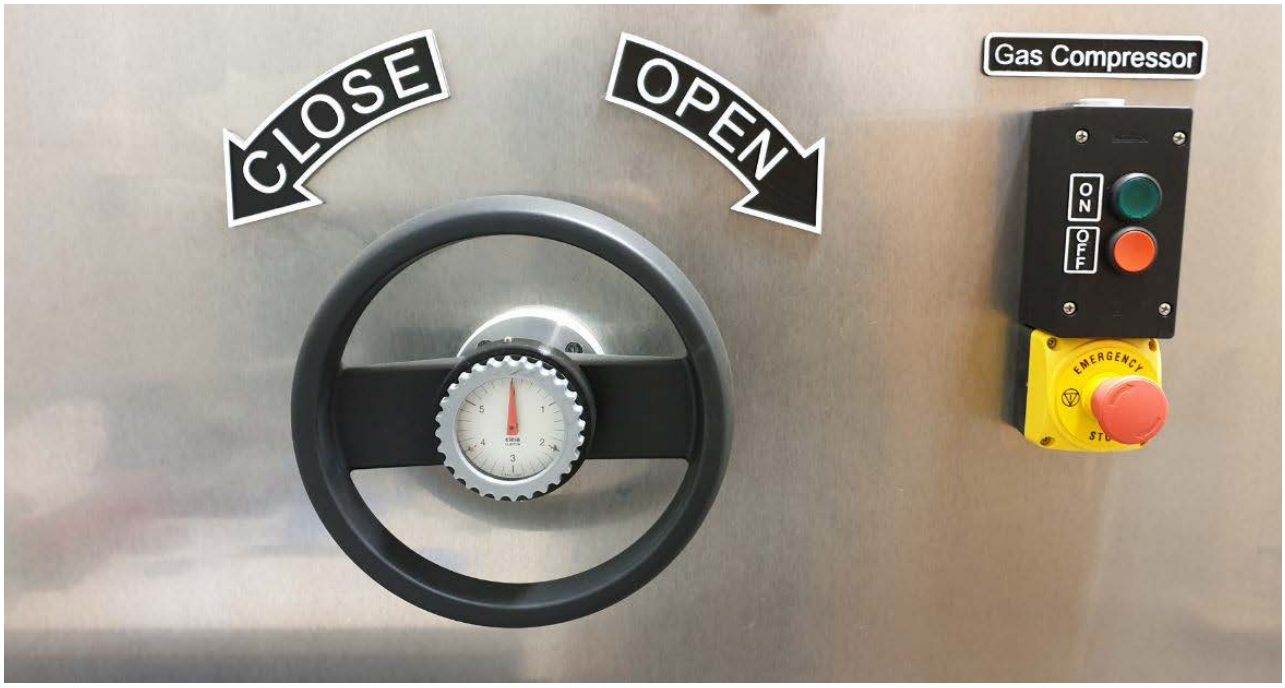

Figure 5 The wheel used to close DACs while inside the pressure chamber and the rotation indicator. ©Stefan Knesz

Before starting this study the gas loading system had only been briefly tested on DACs using standard cut diamond anvils. It quickly became apparent that DACs using Böhler-Almax diamond anvils were not able to be loaded successfully. The clamp which is used to hold the DAC together to fix the screws could not be tightened far enough. A few experiments, to try and make a small gasket imprint using the clamp were done, but failed. The force applied by the wheel (Figure 5) was too strong for a 2 mm pin, which was used as a transmission, and after a few experiments it failed. It had to be replaced by a 3 mm pin which could withstand the force. After changing the pin, the only problems encountered were when the DAC was only opened by about half a rotation, which was easily solved by opening it by a three quarter rotation.

2.2. RAMAN SPETROSCOPY AND RUBY LUMINESCENCE

A Horiba Jobin-Yvon LabRAM HR800 Raman spectrometer was used to obtain the Raman spectra of *α-PbAlBO$_4$* and the Luminescence spectra of the ruby spheres. A 633 nm excitation laser and 1800 grid were used. To focus the beam on the crystal an 50x LWD objective was used. Data acquisition was done with Labspec6 (*HORIBA Scientific*), while PeakFit v4.12 (*Systat Software, Inc.*) was used to fit the spectra.

The position of the R_1 luminescence line of the ruby spheres was used to derive pressure following an experimentally determined equation (Mao et. al. 1986). At a pressure of 1 atm it occurs at around 694,44 nm. The R_1 of most rubies was measured and used at 694,3 nm for pressure

calculations however. While the typical red color of ruby is caused by Cr^{3+} impurities in corundum lattice (Al_2O_3) which substitute for Al^{3+}, the R_1 line is caused by the transition of electrons of Cr^{3+} from excited state to ground state (Sugano and Tanabe, 1958).

With rising pressure the position of the R_1 line is red shifting. The empirical formula

$$P = \frac{A}{B}\left\{\left[1+\left(\frac{\Delta\lambda}{\lambda_0}\right)\right]^8 - 1\right\} \quad \text{(Equation 1)}$$

was used to calculate the pressure in Mbar, where A = 19.04 Mbar, B = 7.665 and λ is the wavelength of the R_1 line (Mao et. al. 1986). Wherever X-ray measurements were made the pressure was determined more precisely by using the unit cell volume of quartz (see section 2.4).

2.3. X-RAY DIFFRACTOMETRY

In this study two types of diffractometers were used. To obtain the orientation matrices of *α-$PbAlBO_4$* crystals and quartz crystals a STOE StadiVari diffractometer was used. The STOE StadiVari has an open Eulerian Cradle and is equipped with a MoKα microfocus X-ray tube and a Dectris PILATUS 300K detector. X-Area 1.7.2 (Stoe & Cie, 2002) was used for instrument control, data acquisition and processing of measured frames.

The lattice parameters of $PbAlBO_4$ and quartz crystals were obtained using a STOE AED2 four-circle diffractometer. The STOE AED2 has a full Eulerian Cradle and is equipped with a MoKα fine focus X-ray tube and a scintillation point detector. SINGLE (Angel & Finger, 2011) was used for instrument control, data acquisition and processing of measured step scans. The DACs *φ* -axis was fixed during measurement. At each pressure step the orientation matrix of both *α-$PbAlBO_4$* and quartz was updated using data from a 2 position-centering of two reflections. To accurately determine unit-cell parameter of *α-$PbAlBO_4$* and quartz, 8 position-centering of a list of reflections was applied (King and Finger, 1979). Both unconstrained and constrained vector least square refinements were performed in order to obtain lattice parameters fitted to the XRD setting angles.

The unit-cell volume of quartz was put into a 4^{th} – order Birch-Murnaghan-Equation of state, using EoSFit7 PV/PVT Calculator, to determine the pressure (Scheidl et al, 2016).

2.4. EQUATION OF STATE

The change of unit-cell parameters of a crystalline material with changing pressure can be described by an Equation of State (EoS). The Birch-Murnaghan-EoS (Equation 2) was developed by adding a finite strain to the Murnaghan-EoS (Birch, 1947).

$$P = 3K_0 f_E(1+2f_E)^{5/2}\left(1+\frac{3}{2}(K'-4)f_E+\frac{3}{2}\left(K_0K''+(K'-4)(K'-3)+\frac{35}{9}\right)f_E^2\right) \quad \text{(Equation 2)}$$

For a Birch-Murnaghan-EoS of second order *K´* has to take the fixed value of *K' = 4* to omit higher orders. For a 3rd – Birch-Murnaghan-EoS *K´* is a free variable, therefore it is implied that *K´´* has a value since *K´* is not constant anymore (Angel et al., 2000).

EoSFit7_GUI (Gonzalez-Platas, 2016) was used to fit the observed X-ray data to determine a Birch-Murnaghan-EoS for *α-PbAlBO$_4$*.

3. RESULTS

3.1. X-RAY DIFFRACTOMETRY

Unit-cell parameters of *α-PbAlBO₄* were measured from 0.24 to 23.09 GPa. The total decrease of the *a*- and *b*-axis up to 23.09 GPa was ~3.85 % and 9.58 %, respectively. Negative axial compressibility of the *c*-axis was observed, with an initial expansion of ~2 % up to ~4 GPa and a decrease by ~0.24 % from maximum expansion to maximum pressure. The last pressure calculation using the unit-cell volume of Quartz was done at 19.07 GPa (Table 1) as it experiences an amorphization over the range of 15 – 30 GPa (Richet & Gillet, 1997, Kingma et al, 1993, Campañá et al, 2004). After the highest pressure step at ~23 GPa two decompression steps at ~15 and ~10 GPa, as well as 4 re-compression steps were obtained. All of those pressure calculations including one pressure point at ~8 GPa were obtained by using the R_1-line of ruby (Mao et. al. 1986) (Table 2).

V_{Quartz} [Å³]	P [GPa]	*a* [Å]	*b* [Å]	*c* [Å]	V [Å³]
112.241(10)	0.244(3)	5.7417(9)	6.9472(5)	8.0558(5)	321.34(6)
112.109(68)	0.290(24)	5.7403(7)	6.9348(6)	8.0693(10)	321.22(4)
111.725(27)	0.425(10)	5.7378(5)	6.9254(5)	8.0708(9)	320.70(4)
111.083(24)	0.658(9)	5.7349(5)	6.9079(9)	8.0648(11)	319.49(6)
110.843(28)	0.748(10)	5.7332(5)	6.9025(4)	8.0720(8)	319.44(3)
110.002(21)	1.074(8)	5.7286(5)	6.8810(4)	8.0716(7)	318.17(3)
108.642(19)	1.640(8)	5.7199(4)	6.8454(4)	8.0733(6)	316.11 (3)
108.315(25)	1.783(11)	5.7180(5)	6.8377(4)	8.0730(7)	315.64(3)
107.914(25)	1.962(11)	5.7158(5)	6.8270(4)	8.0733(7)	315.03(3)
106.818(37)	2.477(18)	5.7083(5)	6.7968(4)	8.0744(8)	313.27(3)
105.847(19)	2.961(10)	5.7024(6)	6.7702(5)	8.0740(9)	311.71(4)
105.292(13)	3.251(3)	5.6979(10)	6.7647(16)	8.0625(13)	310.76(10)
104.249(24)	3.821(13)	5.6935(23)	6.7341(23)	8.0752(37)	309.61(19)
103.797(28)	4.080(16)	5.6878(5)	6.7132(4)	8.0733(9)	308.27(4)
103.178(8)	4.444(5)	5.6824(25)	6.7003(3)	8.0675(7)	307.16(3)
101.335(26)	5.607(17)	5.6684(5)	6.6455(5)	8.0724(10)	304.08 (4)
100.610(5)	6.098(4)	5.6635(10)	6.6340(13)	8.0612(9)	302.88(9)
100.021(25)	6.511(17)	5.6581(5)	6.6104(4)	8.0681(9)	301.76 (4)
99.851(23)	6.633(17)	5.6563(10)	6.6104(11)	8.0766(28)	301.99(11)
99.137(15)	7.156(12)	5.6505(5)	6.5863(5)	8.0653(10)	300.16(4)
98.529(12)	7.618(9)	5.6447(3)	6.5719(3)	8.0646(10)	299.17(4)
97.123(6)	8.743(5)	5.6368(61)	6.5386(23)	8.0427(31)	296.44(33)
97.088(9)	8.771(8)	5.6324(4)	6.5376(5)	8.0527(12)	296.52(5)
93.286(31)	12.25(3)	5.5983(10)	6.4513(13)	8.0399(33)	290.37(13)
90.135(61)	15.65(7)	5.5748(16)	6.3729(17)	7.9907(58)	283.89(19)
87.36(11)	19.06 (14)	5.5432(23)	6.3207(30)	7.9672(67)	279.15(26)

Table 1 Unit-cell parameters of *α-PbAlBO₄* with Pressure as indicated by the quartz and its unit-cell volume.

$R_{1\ (Ruby)}$ [cm^{-1}]	P [GPa]	a [Å]	b [Å]	c [Å]	V [Å³]
697.436(7)	8.73(2)	5.6324(4)	6.5376(5)	8.0527(12)	296.52(5)
697.963(8)	10.22(2)	5.6235(17)	6.5100(17)	8.0434(46)	294.46(18)
698.113(12)	10.65(34)	5.6146(9)	6.4889(28)	8.0417(28)	292.98(11)
698.479(2)	11.69(1)	5.6064(8)	6.4697(7)	8.0369(21)	291.51(8)
699.010(9)	13.21(3)	5.5895(8)	6.4291(7)	8.0206(25)	288.22(9)
699.774(8)	15.41(2)	5.5734(8)	6.3918(9)	8.0032(27)	285.11(10)
699.816(9)	15.53(3)	5.5707(16)	6.3888(13)	7.9971(43)	284.62(16)
702.398(6)	23.09(2)	5.5204(36)	6.2819(55)	7.9175(77)	274.57(34)

Table 2 Unit-cell parameters of *α-PbAlBO₄* with pressure as indicated by the ruby and its R_1 line.

Evolution of the unit-cell parameters can be seen in Figure 6 to Figure 9.

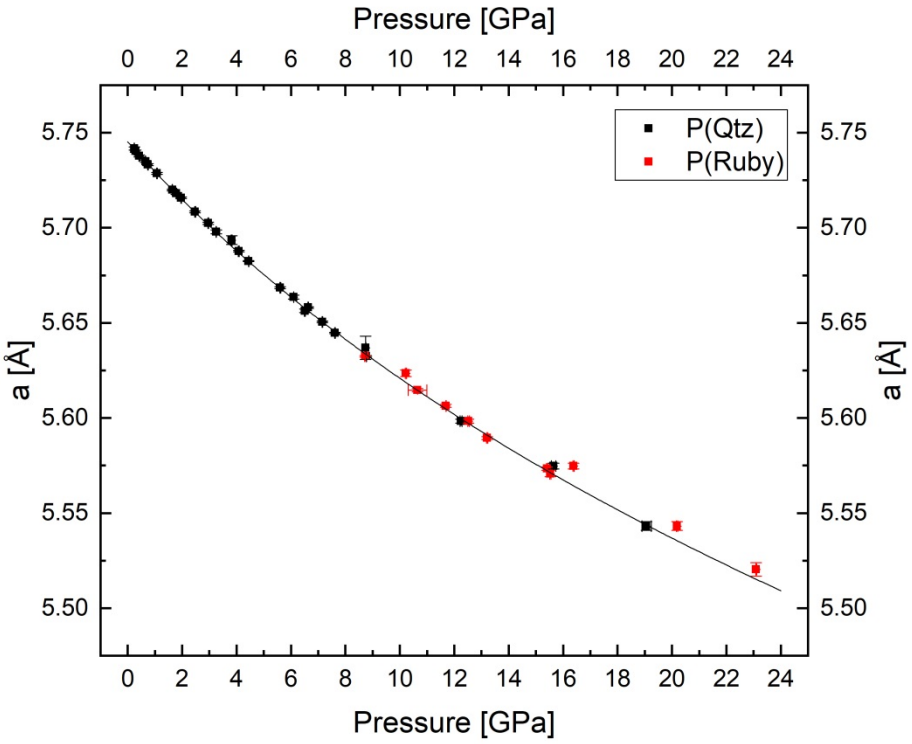

Figure 6 Unit-cell parameter *a* with increasing pressure. Most error bars are smaller than the symbol size. The solid line indicates a fitted 3rd – order Birch-Murnaghan equation of state (see Table 3).

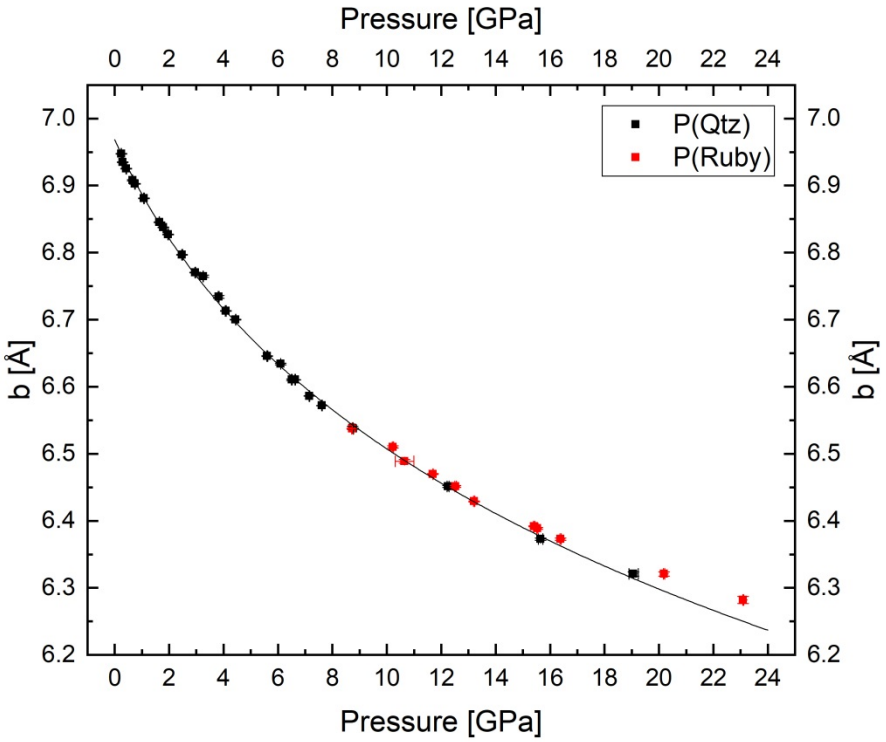

Figure 7 Unit-cell parameter *b* with increasing pressure. Error bars are smaller than the symbol size. The solid line indicates a fitted 3rd – order Birch-Murnaghan equation of state (see Table 3).

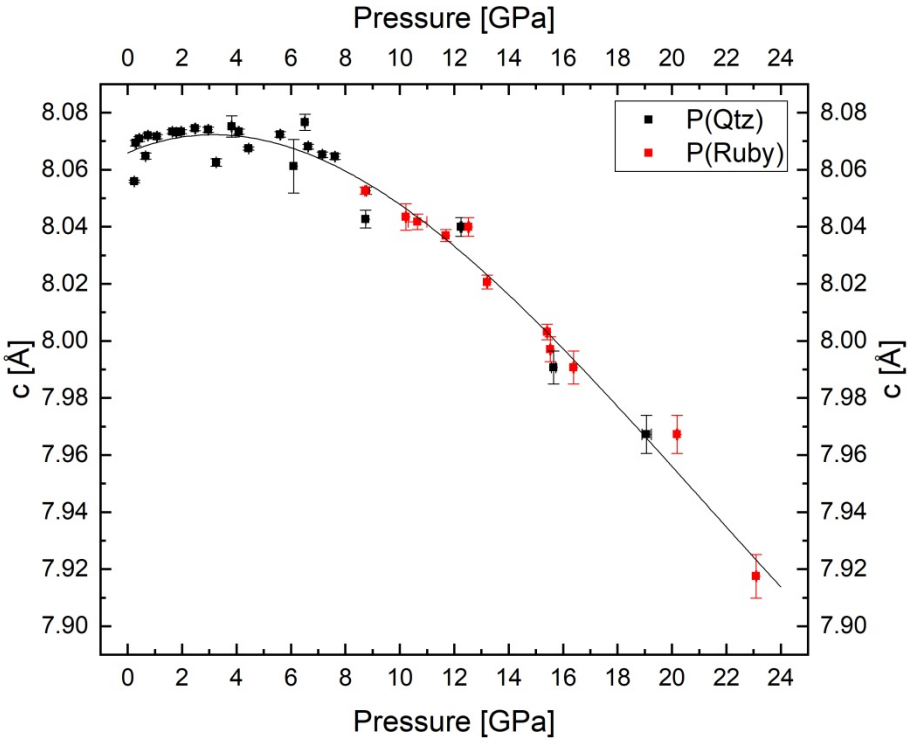

Figure 8 Unit-cell parameter *c* with increasing pressure. Some error bars are smaller than the symbol size. Due the the occuring negative axial compressibility no equation of state could be fitted. Therefore a second degree polynomial function has been fitted (see Table 3).

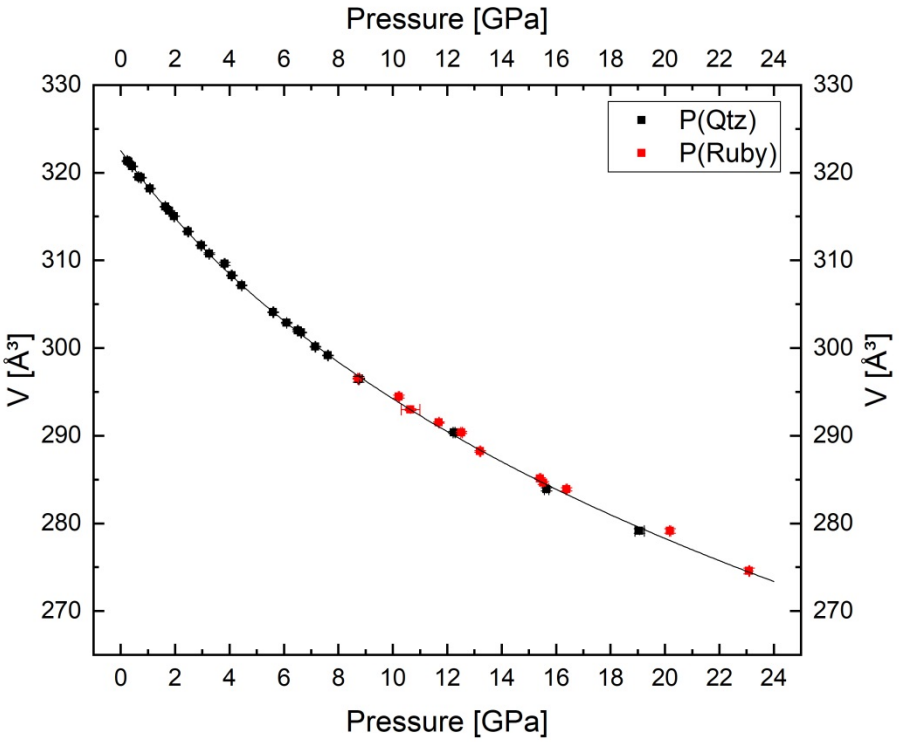

Figure 9 Unit-cell volume Unit-cell increasing pressure. Error bars are smaller than the symbol size. The solid line indicates a fitted 3rd – order Birch-Murnaghan equation of state (see Table 3).

The resulting equations of state are as follows in Table 3.

Unit-cell Parameter	V_0 [Å³]	K_0 [GPa]	K'
V	322.51(8)	74.6(1.0)	8.6(3)
Unit-cell Parameter	L_0 [Å]	M_0 [GPa]	M'
a	5.7452(4)	355(5)	23.6(1,1)
b	6.9687(30)	76(2.5)	19.3(9)
Unit-cell Parameter	*a* [Å*GPa^{-2}]	*b* [Å*GPa^{-1}]	*c* [Å]
c	-7*10$^{(-4)}$	4,1*10$^{(-3)}$	8.0659

Table 3 Equation of state parameters for the volume the *a* and *b* axis and the coefficients of the second degree polynomial function fitted to the *c*-axis of *α-PbAlBO₄*.

The equation of state for the unit-cell volume will be closer examinated in Section 4.2.

3.2. RAMAN SPECTROSCOPY

Raman spectra were mostly acquired from a series of compression up to ~ 19 GPa. Only two spectra were acquired on decompression. At each pressure step three spectra of *α-PbAlBO$_4$* were acquired. They differ by a different orientation of the crystal. The orientations were not in respect to crystallographic axes, but to the z-axis of the DAC. The three orientations will be designated *M1* (DAC z-axis normal to the spectrometer), *M2* (DAC z-axis 90° clockwise rotated to *M1*) and *M3* (DAC z-axis 45° clockwise rotated to *M1*). Plots of the spectra were separated at 200cm^{-1} for enhanced visibility of the bands (Figure 10 to Figure 15).

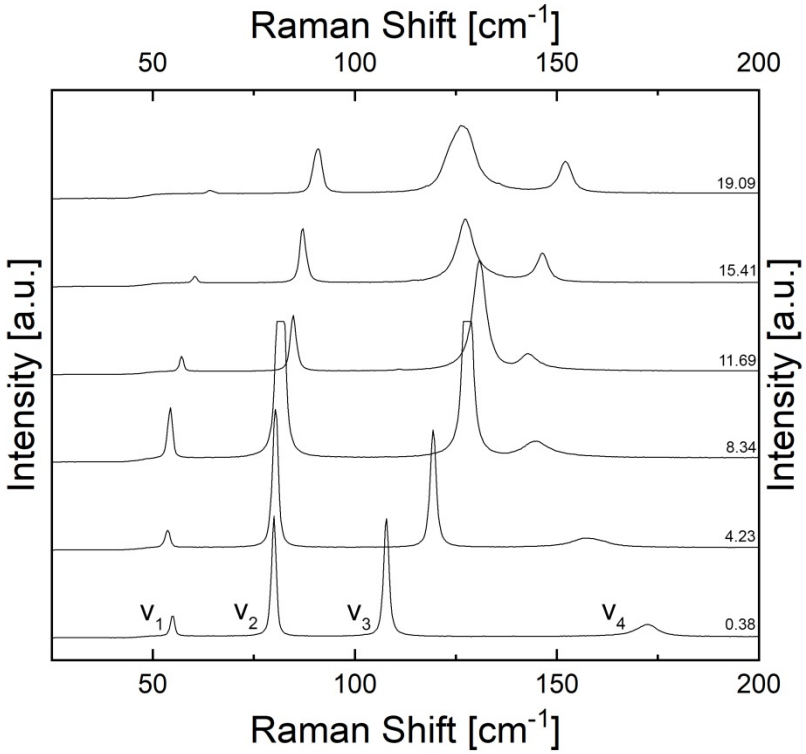

Figure 10 Representative stacked plots of *M1* Raman spectra of *α-PbAlBO$_4$*., demonstrating the evolution of the Raman bands in the spectral range of 25 – 200cm^{-1}. Vertical offset is for representation only.

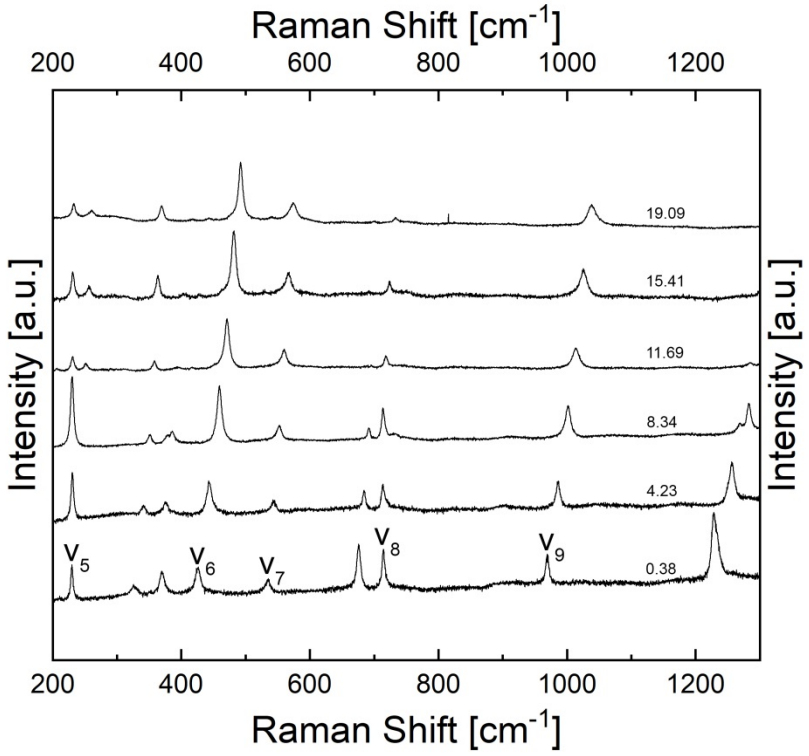

Figure 11 Representative stacked plots of *M1* Raman spectra of *α-PbAlBO$_4$*, demonstrating the evolution of the Raman bands in the spectral range of 200 – 1300cm^{-1}. Vertical offset is for representation only.

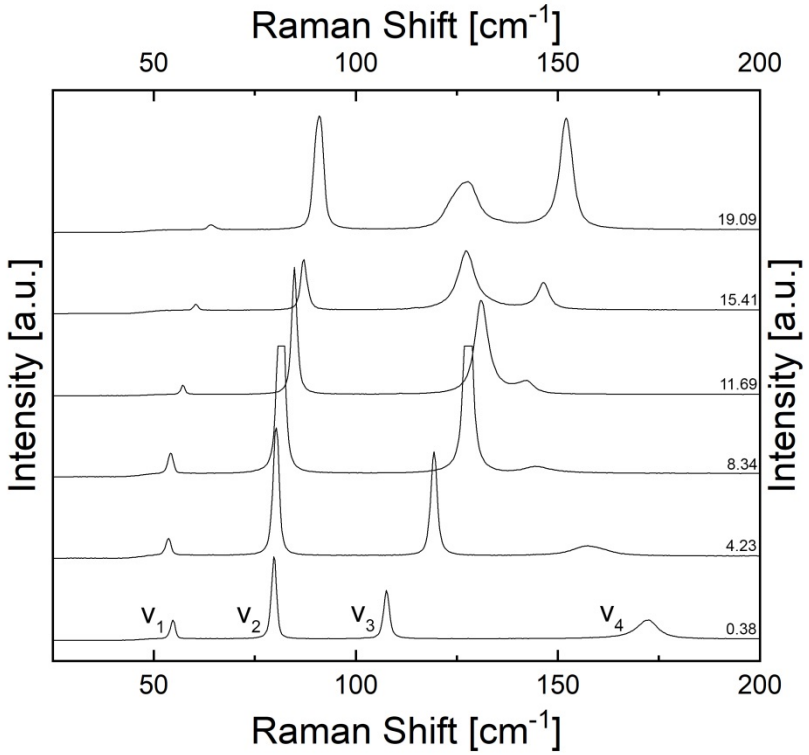

Figure 12 Representative stacked plots of *M2* Raman spectra of *α-PbAlBO$_4$*, demonstrating the evolution of the Raman bands in the spectral range of 25 – 200cm^{-1}. Vertical offset is for representation only.

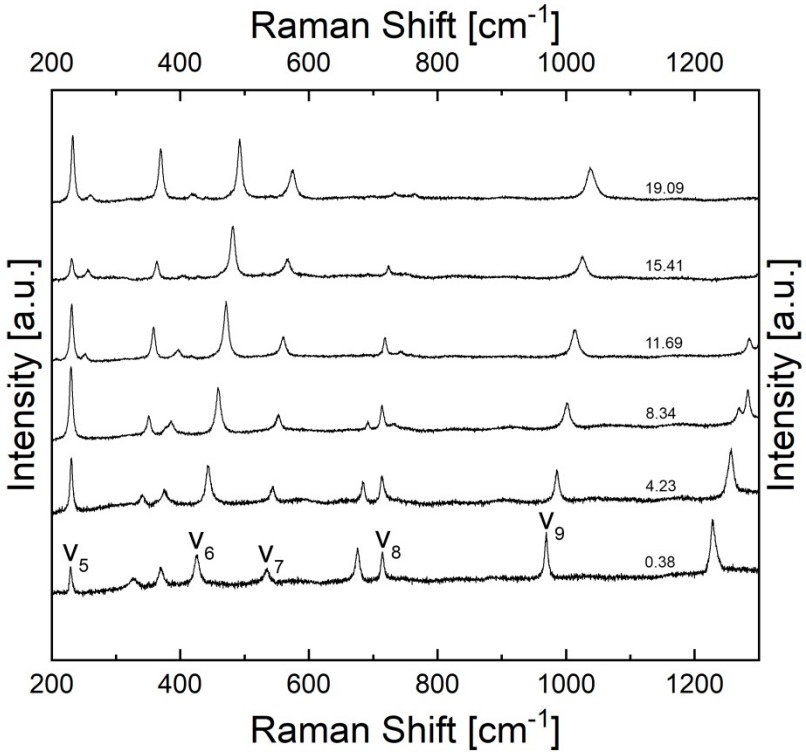

Figure 13 Representative stacked plots of *M2* Raman spectra of *α-PbAlBO$_4$*, demonstrating the evolution of the Raman bands in the spectral range of 200 – 1300cm^{-1}. Vertical offset is for representation only.

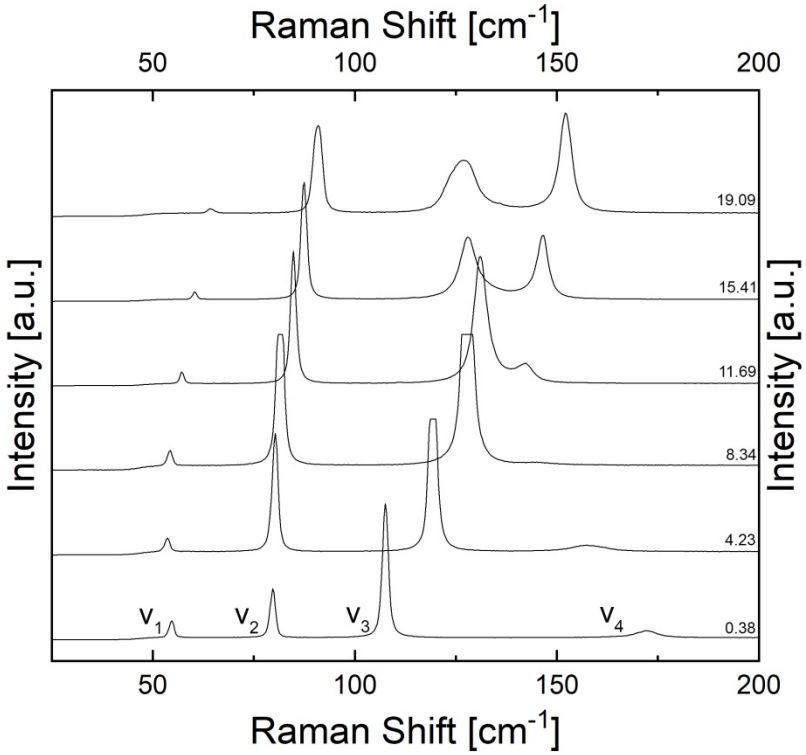

Figure 14 Representative stacked plots of *M3* Raman spectra of *α-PbAlBO$_4$*, demonstrating the evolution of the Raman bands in the spectral range of 25 – 200cm^{-1}. Vertical offset is for representation only.

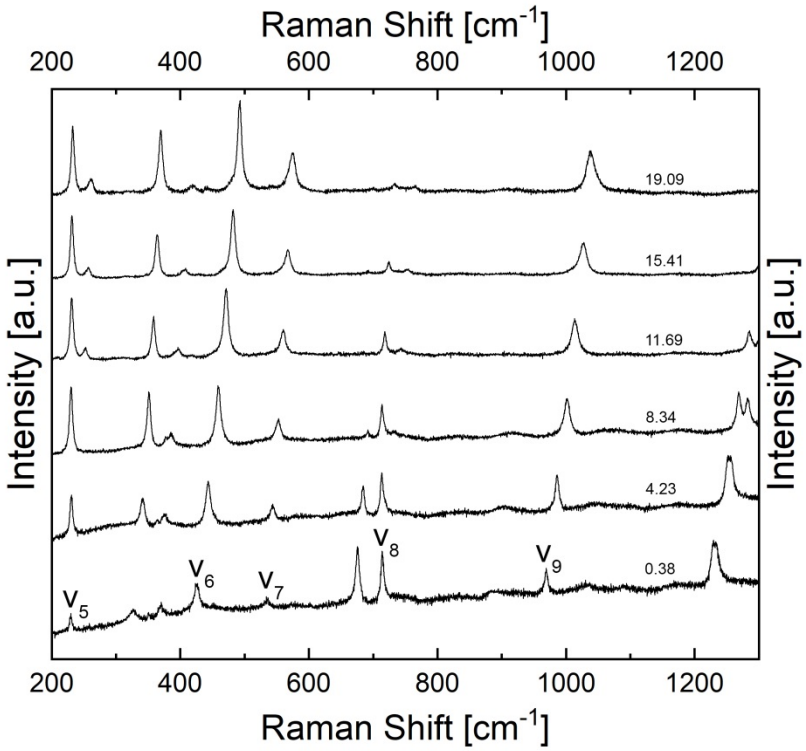

Figure 15 Representative stacked plots of *M3* Raman spectra of *α-PbAlBO$_4$*, demonstrating the evolution of the Raman bands in the spectral range of 200 – 1300cm^{-1}. Vertical offset is for representation only.

The evolution of the nine major Raman bands was plotted to show their position changes with increasing pressure (Figure 16 to Figure 24). Vertical error bars indicate the standard deviation as calculated by the PeakFit software. Error bars are often smaller than the symbol size.

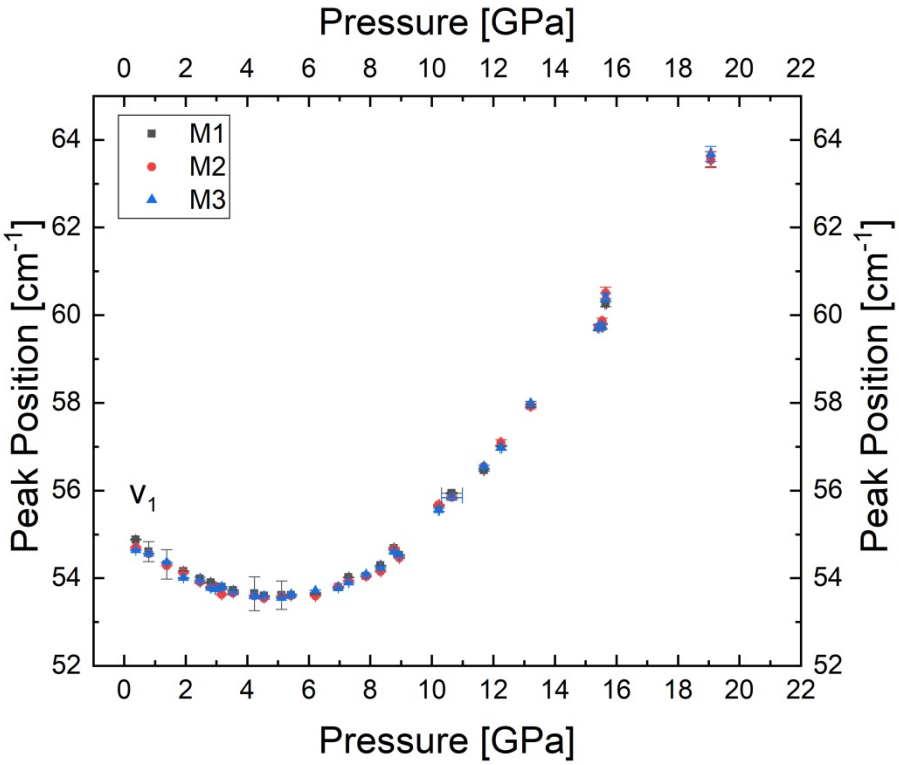

Figure 16 Peak position of the v_1 Raman band at ~54 cm^{-1}.

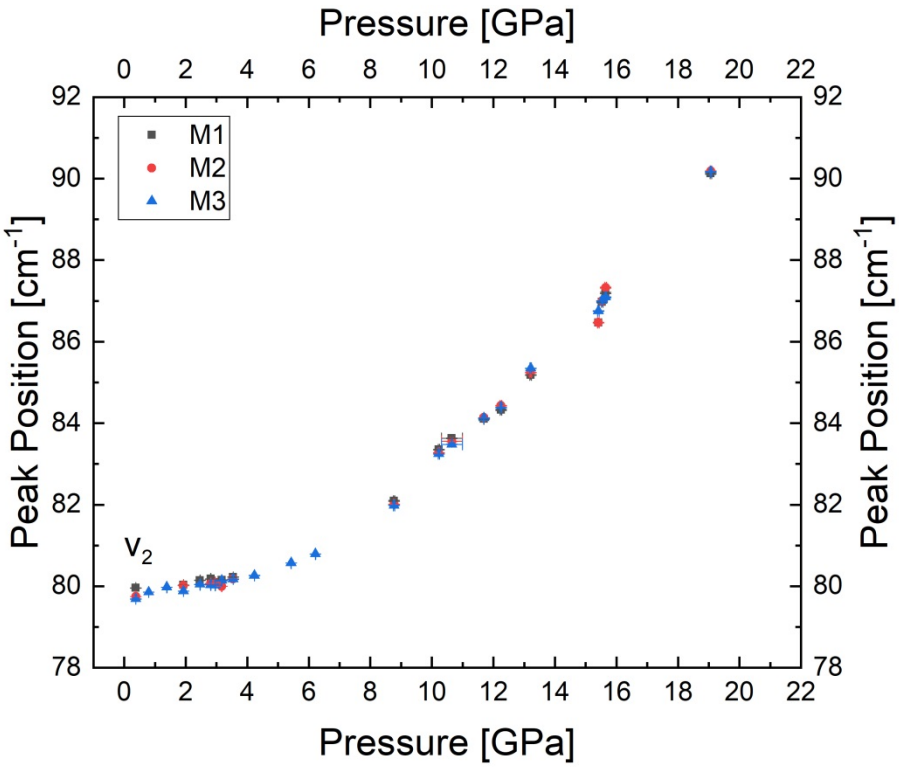

Figure 17 Peak position of the v_2 Raman band at ~80 cm^{-1}.

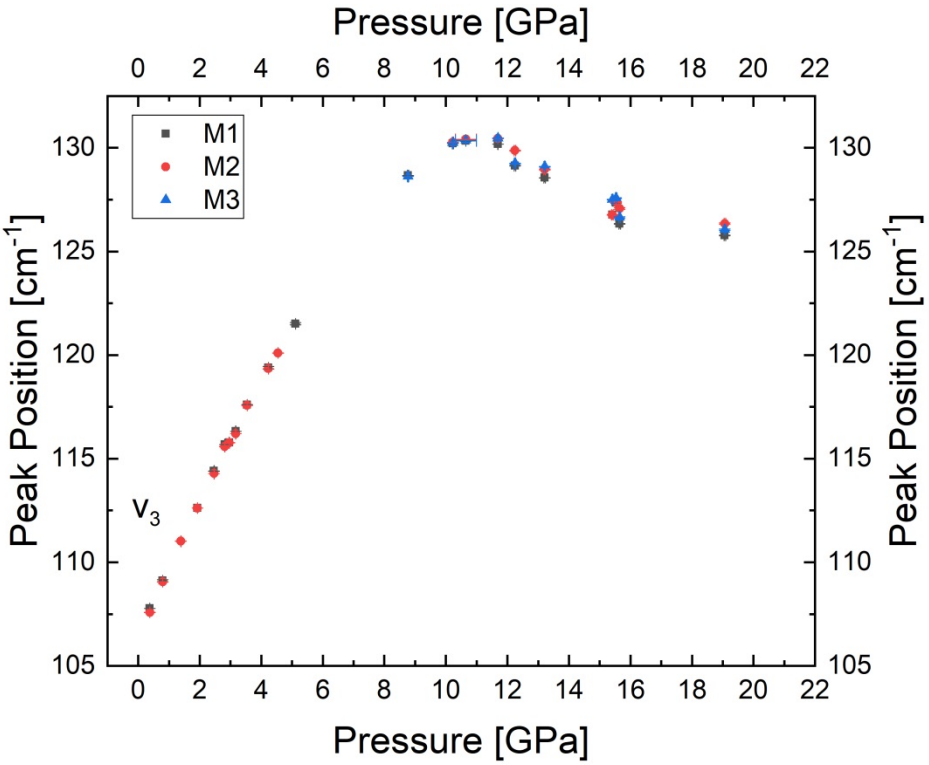

Figure 18 Peak position of the v_3 Raman band at ~107 cm^{-1}.

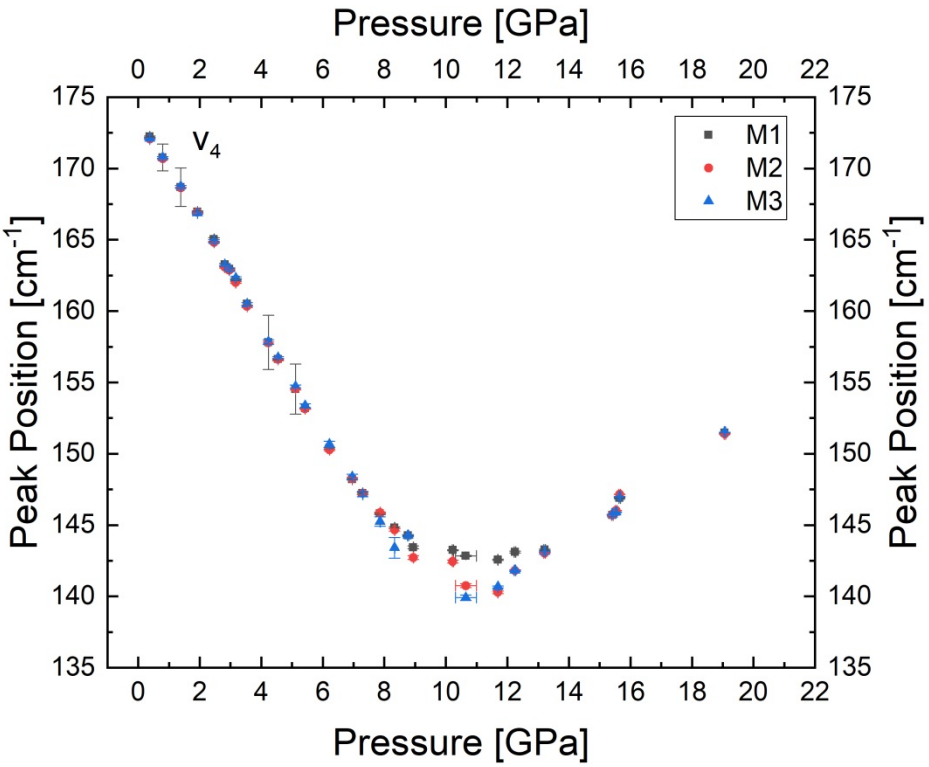

Figure 19 Peak position of the v_4 Raman band at ~172 cm^{-1}.

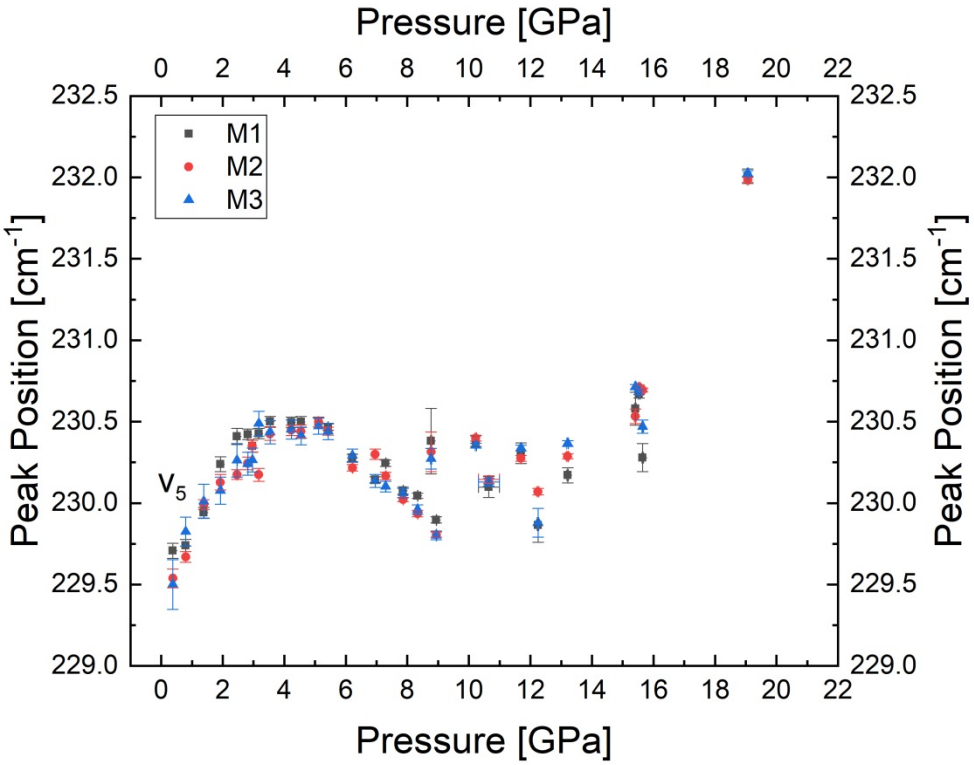

Figure 20 Peak position of the v_5 Raman band at ~230 cm^{-1}.

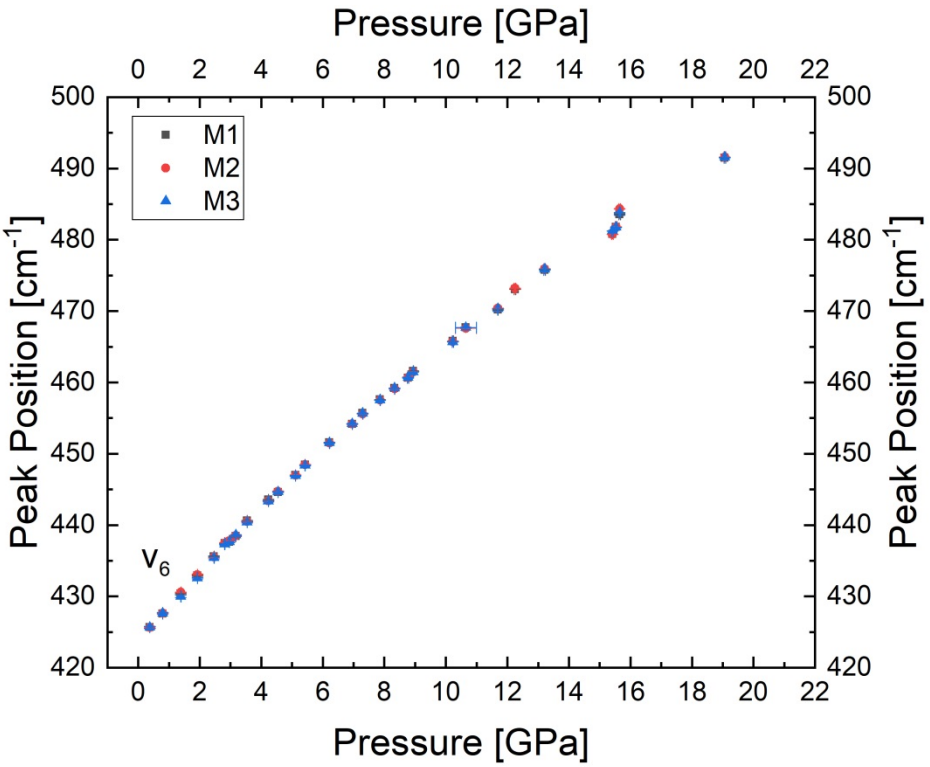

Figure 21 Peak position of the v_6 Raman band at ~425 cm^{-1}.

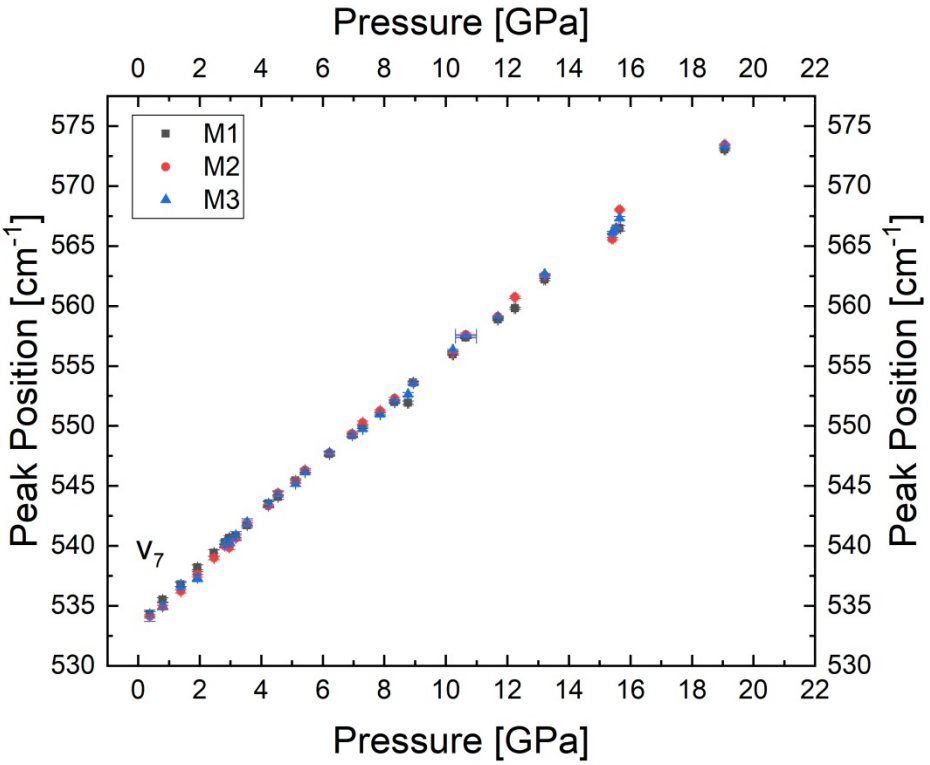

Figure 22 Peak position of the v_7 Raman band at ~534 cm^{-1}.

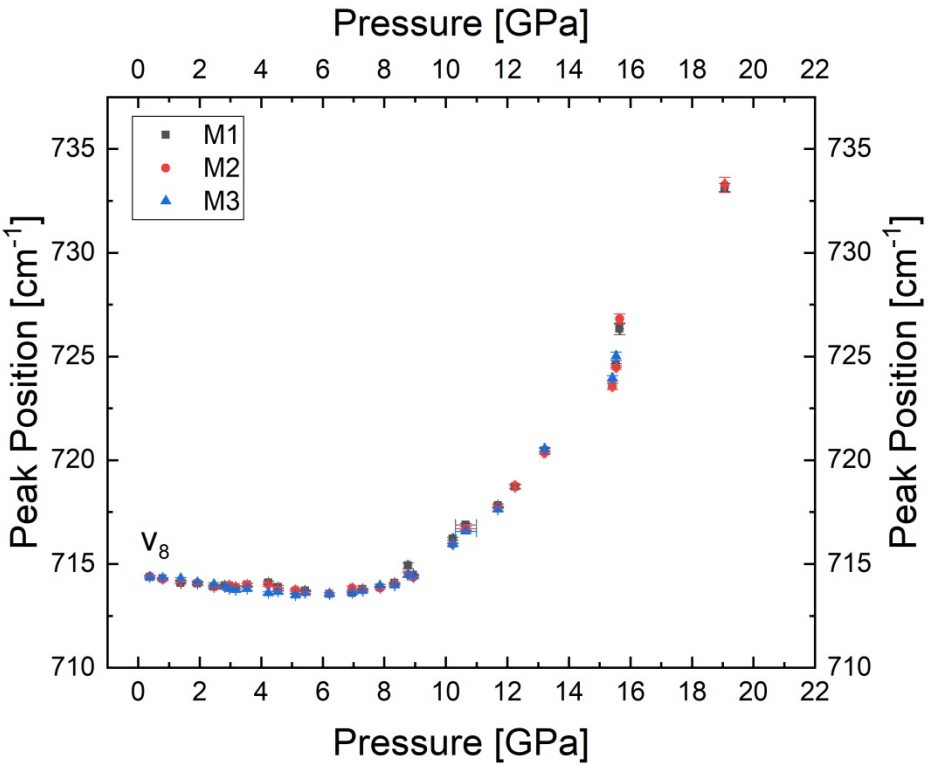

Figure 23 Peak position of the v_8 Raman band at ~714 cm^{-1}.

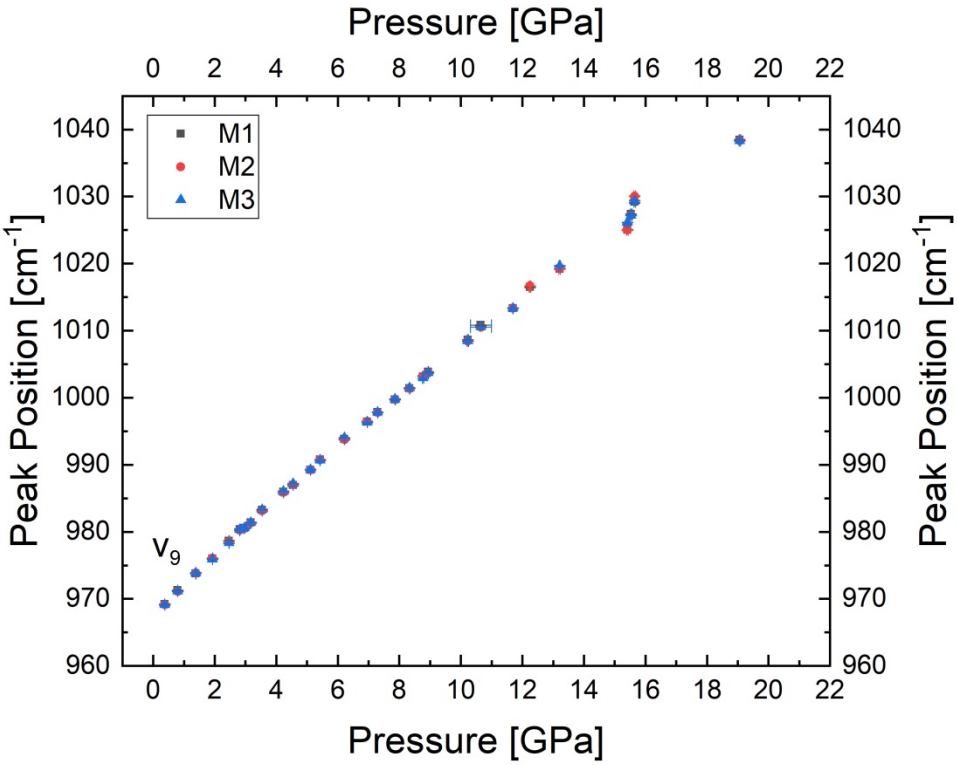

Figure 24 Peak position of the v_9 Raman band at ~969 cm^{-1}.

In almost all Raman bands a small step can be seen at around 15 GPa. This is because pressure calculation using the unit-cell volume of quartz is getting less precise due to quartz nearing its point of amorphization.

4. DISCUSSION

4.1. CHANGES OF RAMAN BANDS

Raman band position at 1bar is in agreement with earlier reported positions. The band assignment was already reported by Gesing et al (2013). The structural units attributed to the heavy atoms show the lowest Raman shift, as expected. According to Gesing et al (2013), the Raman bands v_1 and v_3 (Figure 16 & Figure 18) are Pb-O stretching modes, v_2 (Figure 17) is a Pb-O wagging mode, v_4 (Figure 23) is an O-Pb-O scissoring mode, v_5 (Figure 20) is a Pb-O-Al wagging mode, v_6 (Figure 21) is a mixture of O-Al-O twisting and O-B-O scissoring modes, v_7 and v_8 (Figure 22 & Figure 23) are an O-B-O scissoring mode and v_9 (Figure 24) is a B-O stretching mode.

The Raman bands v_6, v_7 and v_9 experience an almost linear shift while v_1, v_3 and v_4 exhibit a trend reversal. There are two types of Pb-O bonds, one where the bond length is around 2.3 Å (shown as grey coordination polyhedron in Figure 25) and another where the bond length is around 3.3 Å. The stretching of the shorter bonds is represented in Raman band v_1. The evolution of this Raman band correlates well with the negative axial compressibility exhibited by the *c*-axis, which may be the reason for the above mentioned behavior. The evolution of v_2 may be explained by a general compaction of the structure which is also influenced by the negative axial compressibility as the Raman shift of this band is increasing faster after the effect of negative axial compressibility is gone. The asymmetric coordination of the cation is due to a stereochemically active lone electron pair (LEP) which occupies the space in the large cavities opposite to the leads oxygen bonds (Note: The LEP is not shown in the Figure 25). $PbMBO_4$ (M = Al^{3+}, Fe^{3+}, Mn^{3+}) is not the only compound family with mullite-type structure possessing a LEP. $Bi_2M_4O_9$ (M = Al^{3+}, Ga^{3+}, Fe^{3+}) is another family of compounds possessing a LEP, which in this case is located at the Bi^{3+} cation (Schneider, 2012).

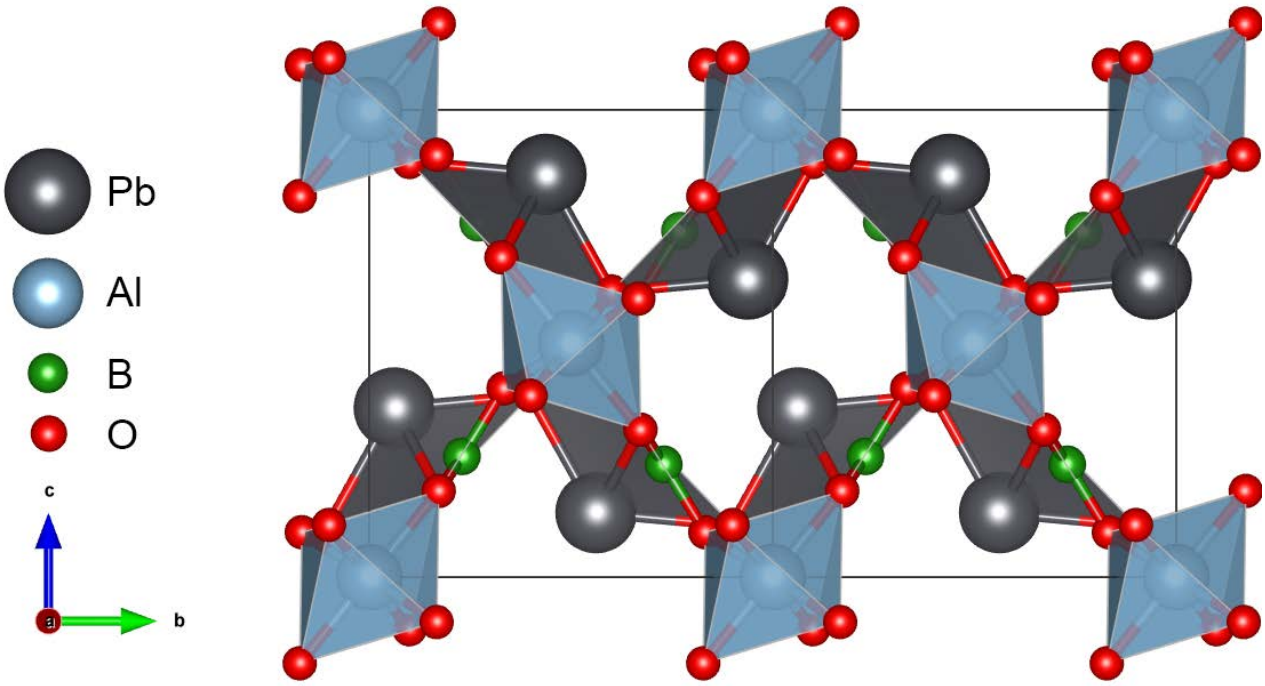

Figure 25 Crystal structure of *α-PbAlBO$_4$* in [100] showing the coordination of the lead atoms and cavities where the LEP is located.

It is proposed that the extraordinary behavior of the v_3 and v_4 Raman bands can be explained by two types of subsequent compression mechanisms in the crystal structure. The first compression mechanism is attributed to the compression of the LEP – cavities. Consequently the LEP is forced closer to the Pb^{2+} cation along with oxygen atoms opposite its coordination polyhedron, which impact the vibration frequency. The second subsequent compression mechanism is a more universal compression with the compaction achieved by the atomic compression of the oxygen atoms and the various more regular PbO_x, AlO_6 and BO_4 building units. The behavior of v_5 may be explained by a combination of negative axial compressibility appearing and disappearing and then the general compaction of structure. The quasi – linear behavior of v_6 v_7 and v_9 can be explained by the general compaction of the structure. It is important to note that the O-B-O scissoring seen in v_7 and v_8 is not the same as v_7 is caused by two bond angles with about 121.3° while v_8 is caused by an angle of 117.5° (Figure 26). The angle in v_8 is therefore relatively constant up to about 7 GPa after which it is decreasing.

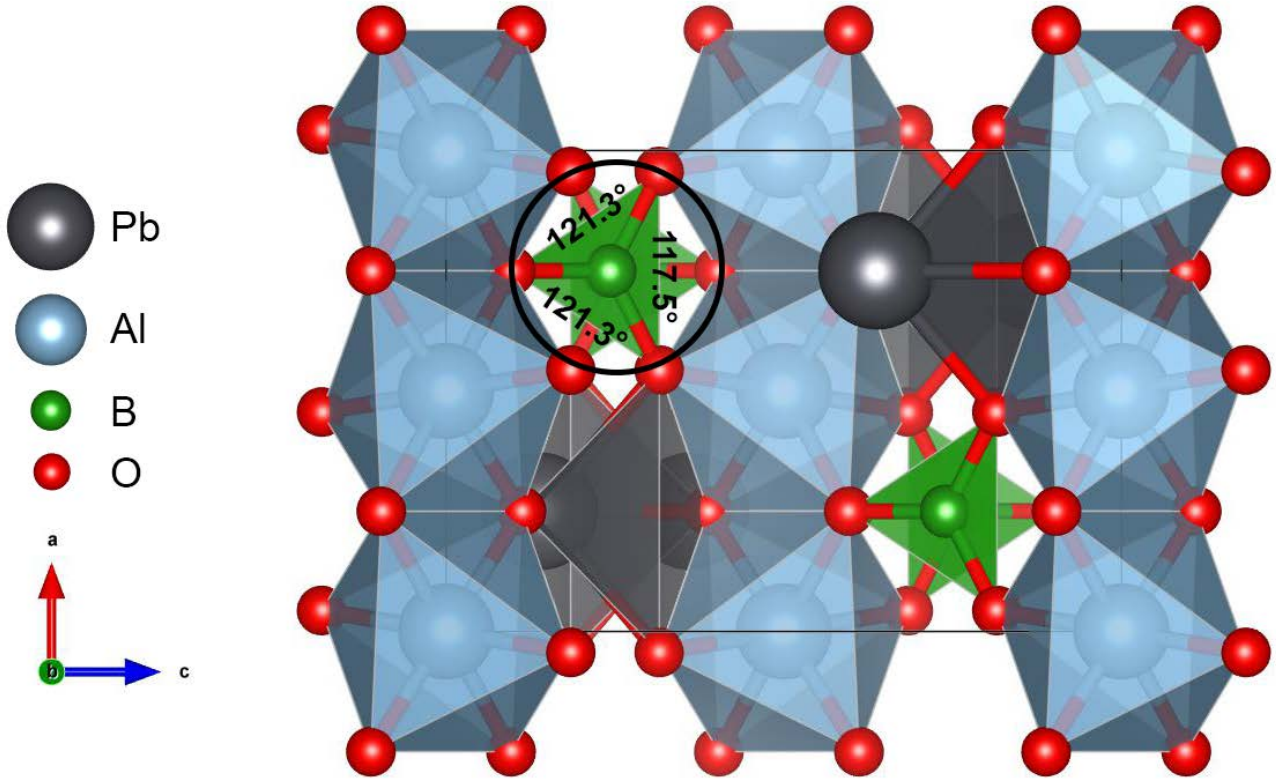

Figure 26 Crystal structure of *α-PbAlBO$_4$* in [010] showing the coordination of the boron atoms and the bond angles.

4.2. EQUATION OF STATE

As shown in Table 3 the fitted equation of state for the unit-cell volume would have a *K'* value of *K' = 8.6(3)* which is high compared to most structurally similar compounds (Table 7). Therefore the data set has been truncated twice. Once between 4.08 GPa and 4.44 GPa and once between 7.62 and 8.74 GPa. For each data point the calculated pressure difference $P_{calc} - P_{obs}$ was plotted against the observed pressure. For the first section this was only done with K' as free variable (Figure 27 and Figure 28). For the second section this was done with *K'* as free parameter as well as *K'* fixed to 5, 6 and 7 (Figure 29 to Figure 36).

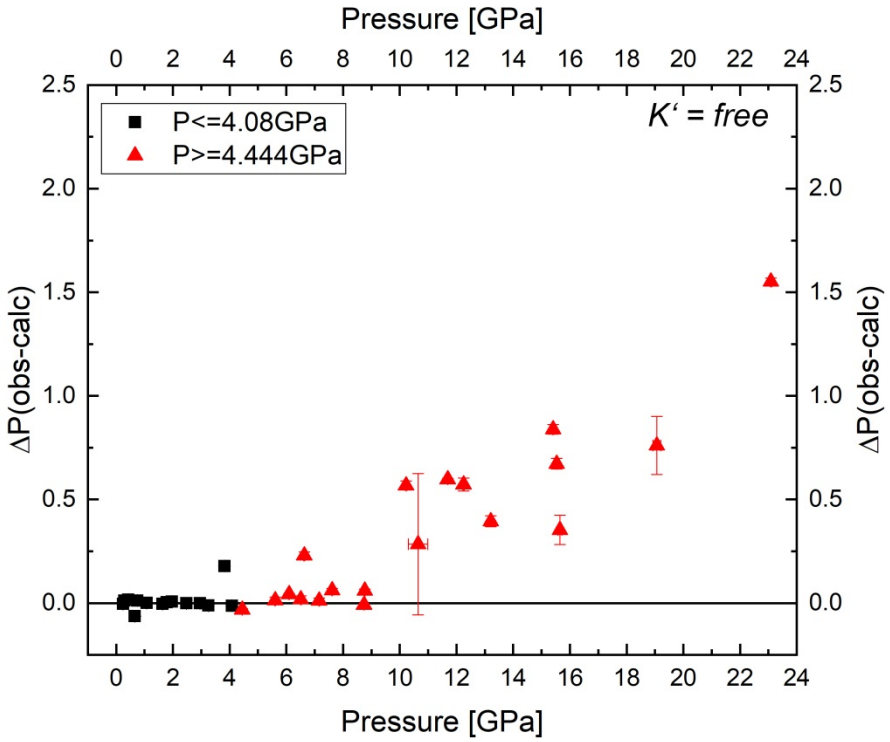

Figure 27 P_{obs} – P_{calc} plot for the first 3rd – order Birch – Murnaghan equation of state with *K'* as a free variable. The truncation here is between 4.08 and 4.44 GPa.

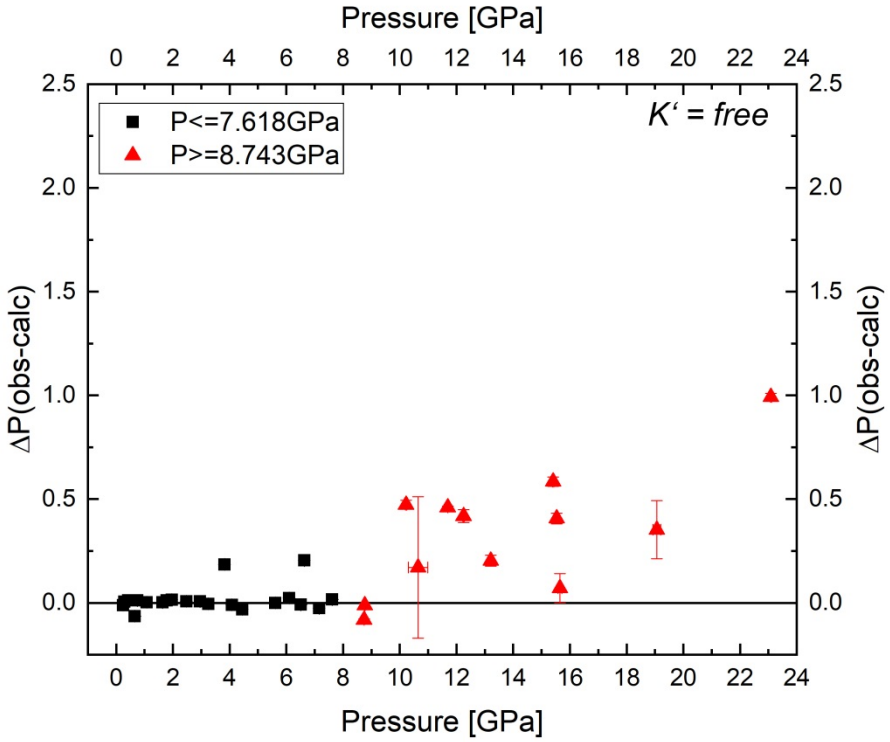

Figure 28 P_{obs} – P_{calc} plot for the first 3rd – order Birch – Murnaghan equation of state with *K'* as a free variable. The truncation here is between 7.62 and 8.74 GPa.

In Table 4 the 3rd – order Birch – Murnaghan equations of state for the two first sections with *K'* as free variable are shown.

V_0 [Å³]	K_0 [GPa]	*K'*	*W-X²*
322.34(7)	79(2)	6.8(1.1)	2.15
322.38(6)	77.5(1.2)	7.4(4)	3.07

Table 4 3rd – order Birch – Murnaghan equations of state for both first sections (truncation between 4.08 and 4.44 GPa and 7.62 and 8.74 GPa) with *K'* as free variable. Additionally the W-X² result as calculated by the EoSFit7_GUI software is shown.

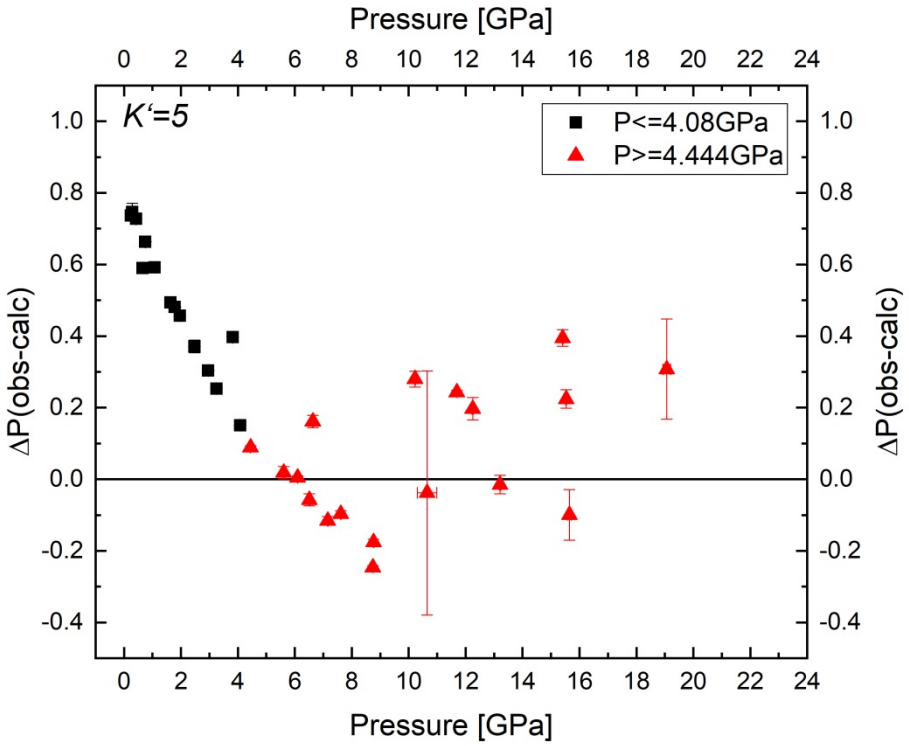

Figure 29 P_{obs} – P_{calc} plot for the second 3rd – order Birch – Murnaghan equation of state with *K'* fixed to *5.* The truncation here is between 4.08 and 4.44 GPa.

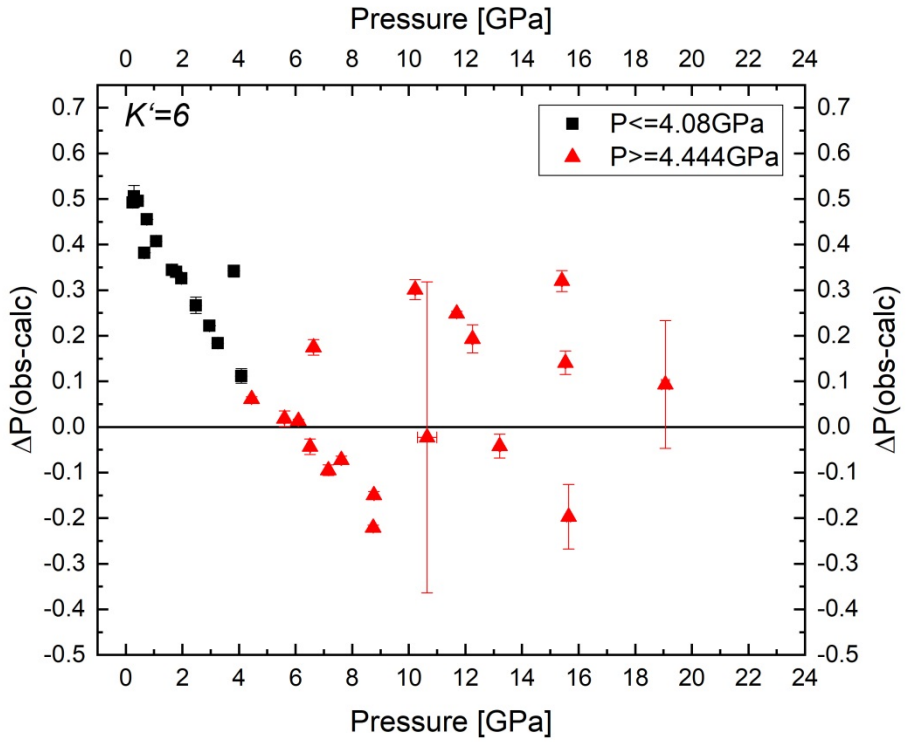

Figure 30 P_{obs} – P_{calc} plot for the second 3rd – order Birch – Murnaghan equation of state with *K'* fixed to *6.* The truncation here is between 4.08 and 4.44 GPa.

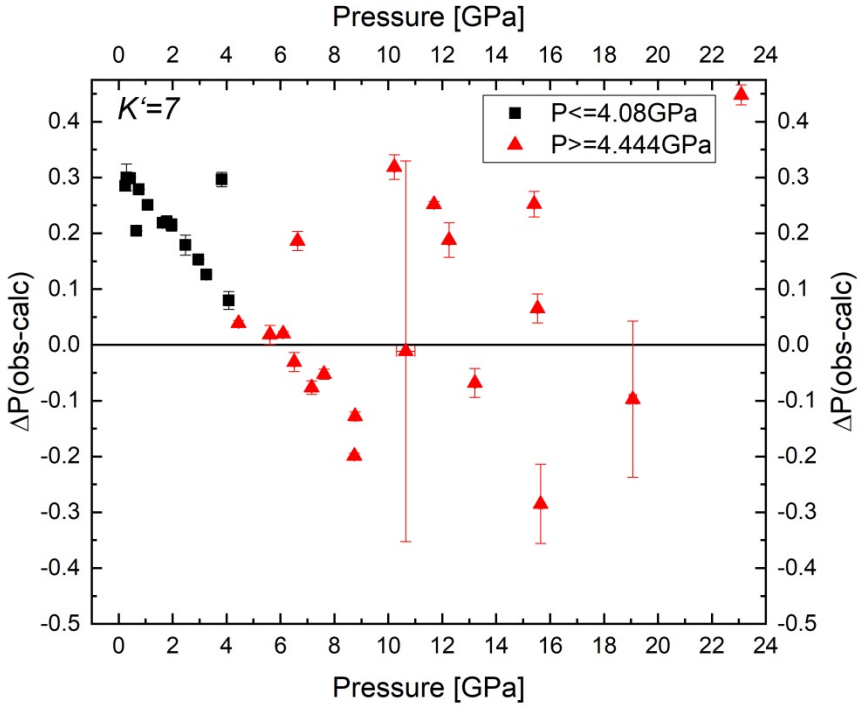

Figure 31 P_{obs} – P_{calc} plot for the second 3rd – order Birch – Murnaghan equation of state with *K'* fixed to *7.* The truncation here is between 4.08 and 4.44 GPa.

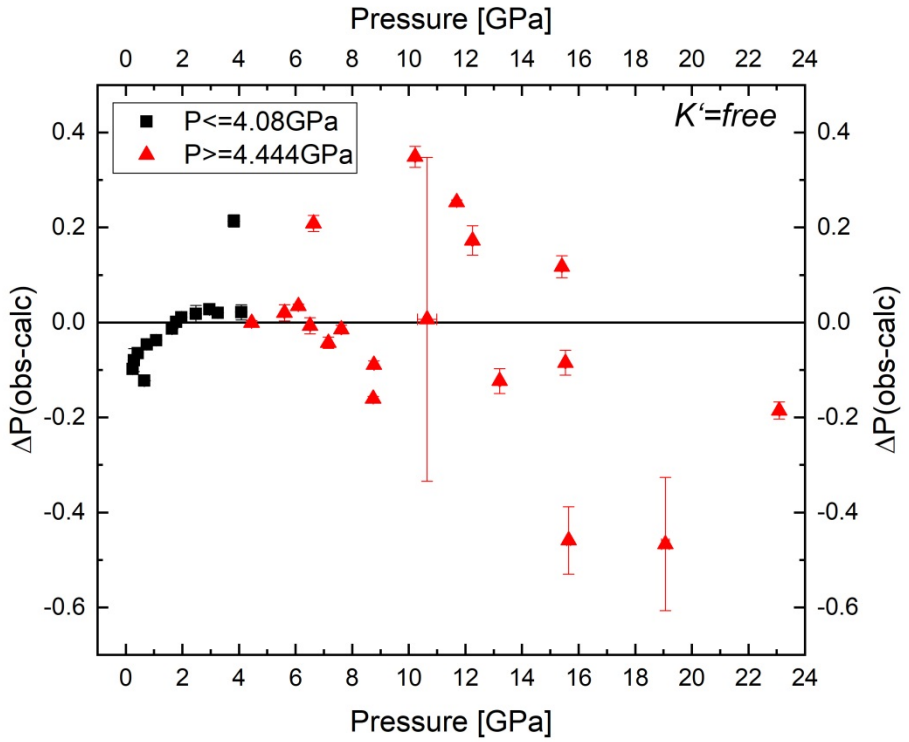

Figure 32 P_{obs} – P_{calc} plot for the second 3rd – order Birch – Murnaghan equation of state with *K'* as a free variable. The truncation here is between 4.08 and 4.44 GPa.

The equations of state for the second 3rd – order Birch – Murnaghan equations of state, with a truncation at 4.08 GPa, for all four *K'* values can be seen in Table 5.

V_0 [Å³]	K_0 [GPa]	*K'*	*W-X²*
319.7(3)	98.3(1.6)	5	17.13
320.5(3)	91.1(1.3)	6	11.96
321.2(2)	84.5(1.1)	7	8.94
322.9(9)	71(6)	9.4(1.3)	7.04

Table 5 3rd – order Birch – Murnaghan equations of state for the second section for all four *K'* values with the truncation done between 4.08 and 4.44 GPa. Additionally the W-X² result as calculated by the EoSFit7_GUI software is shown.

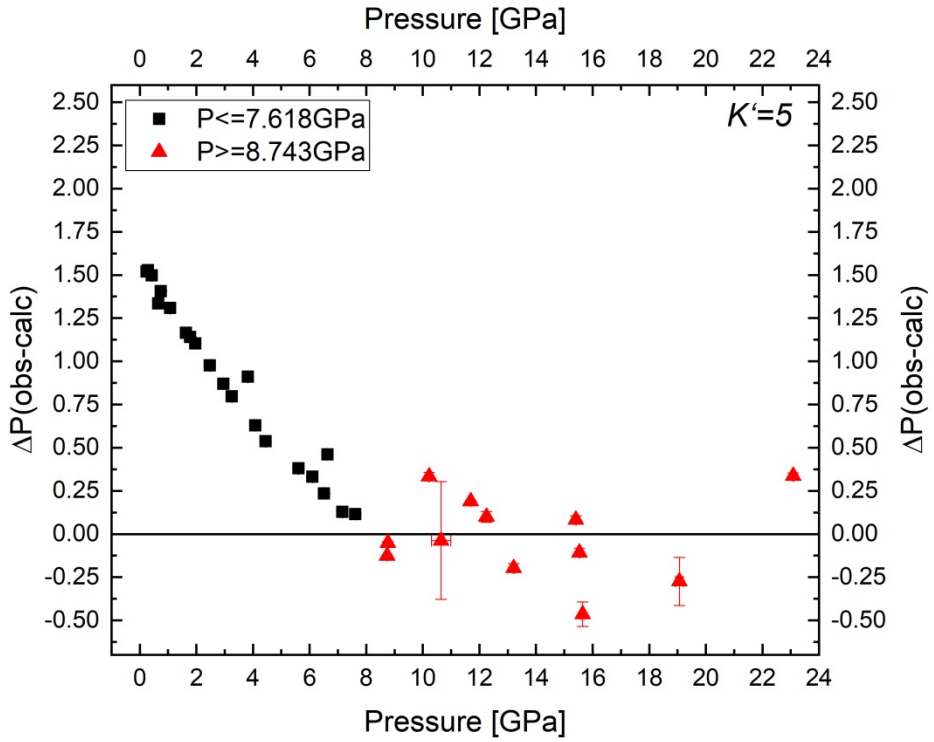

Figure 33 P_{obs} – P_{calc} plot for the second 3rd – order Birch – Murnaghan equation of state with *K'* fixed to *5*. The truncation here is between 7.62 and 8.74 GPa.

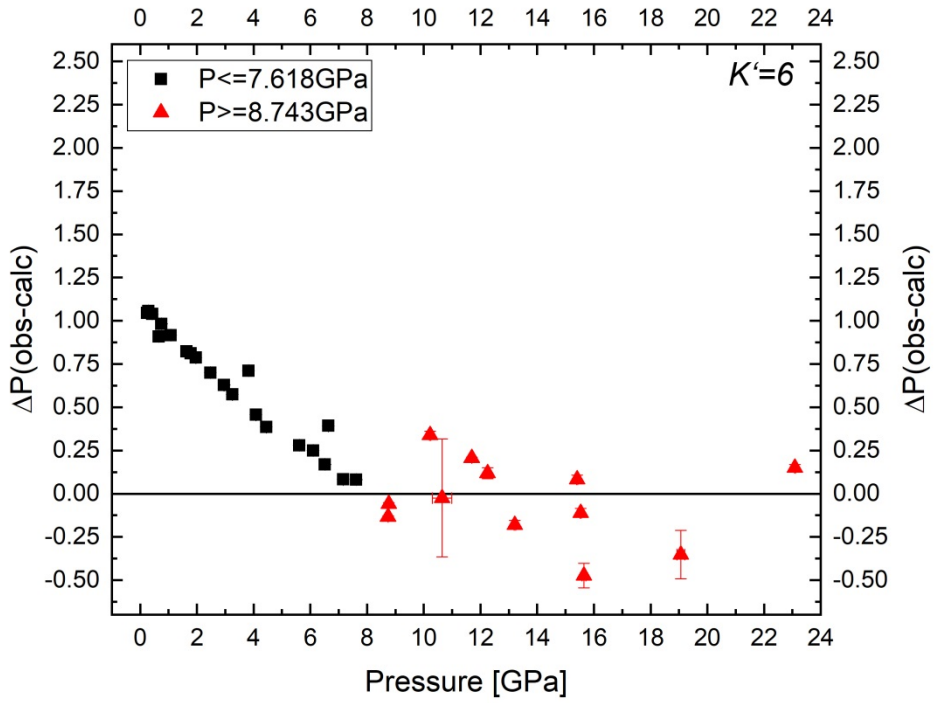

Figure 34 P_{obs} – P_{calc} plot for the second 3rd – order Birch – Murnaghan equation of state with *K'* fixed to *6*. The truncation here is between 7.62 and 8.74 GPa.

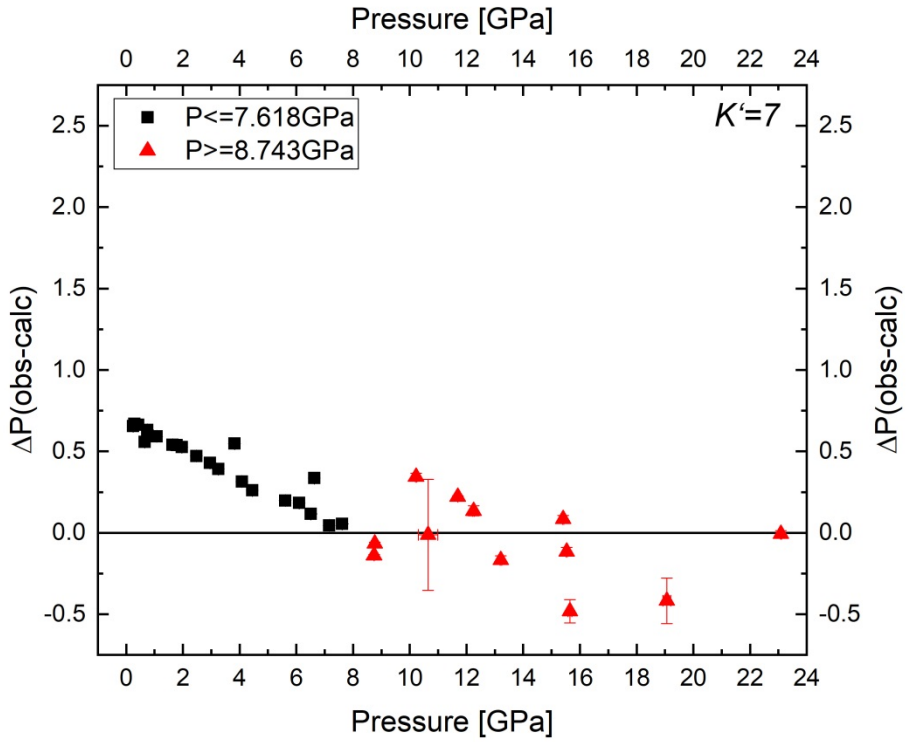

Figure 35 P_{obs} – P_{calc} plot for the second 3rd – order Birch – Murnaghan equation of state with K' fixed to *7*. The truncation here is between 7.62 and 8.74 GPa.

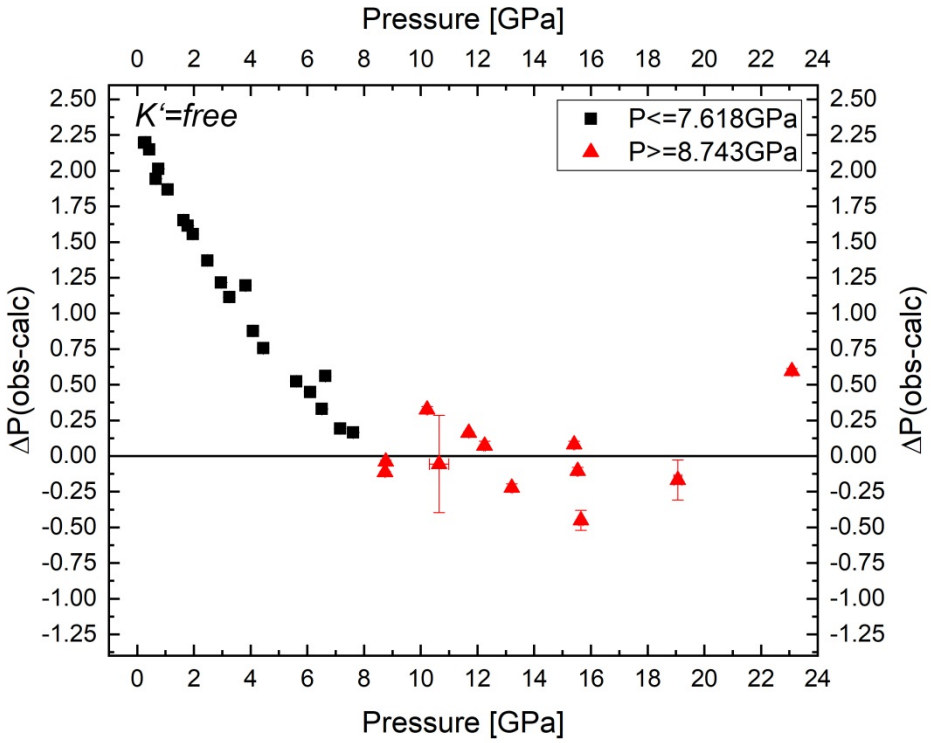

Figure 36 P_{obs} – P_{calc} plot for the second 3rd – order Birch – Murnaghan equation of state with *K'* as a free variable. The truncation here is between 7.62 and 8.74 GPa.

The equations of state for the second 3rd – order Birch – Murnaghan equations of state, with a truncation at 7.613 GPa, for all four *K'* values can be seen in Table 6.

V_0 [Å³]	K_0 [GPa]	*K'*	*W-X²*
317.5(6)	109(3)	5	6.14
318.7(7)	99(3)	6	6.58
319.9(7)	90(3)	7	7.12
316.1(2.3)	122(22)	3.8(1.9)	6.59

Table 6 3rd – order Birch – Murnaghan equations of state for the second section for all four *K'* values with the truncation done between 7.62 and 8.74 GPa. Additionally the W-X² result as calculated by the EoSFit7_GUI software is shown.

In view of the W-X² values it seems sensible to truncate the data set between 7.62 and 8.74 GPa. That is why the first 3rd – order Birch – Murnaghan equation of state is proposed to be V_0 = 322.38(6) Å³, K_0 = 77.5(1.2) GPa and *K'* = 7.4(4). For the second equation of state the values of V_0 = 317.5(6) Å³, K_0 = 109(3) GPa and *K'* = 5 are proposed. The unit-cell volume and both calculated equations of state are shown in Figure 37.

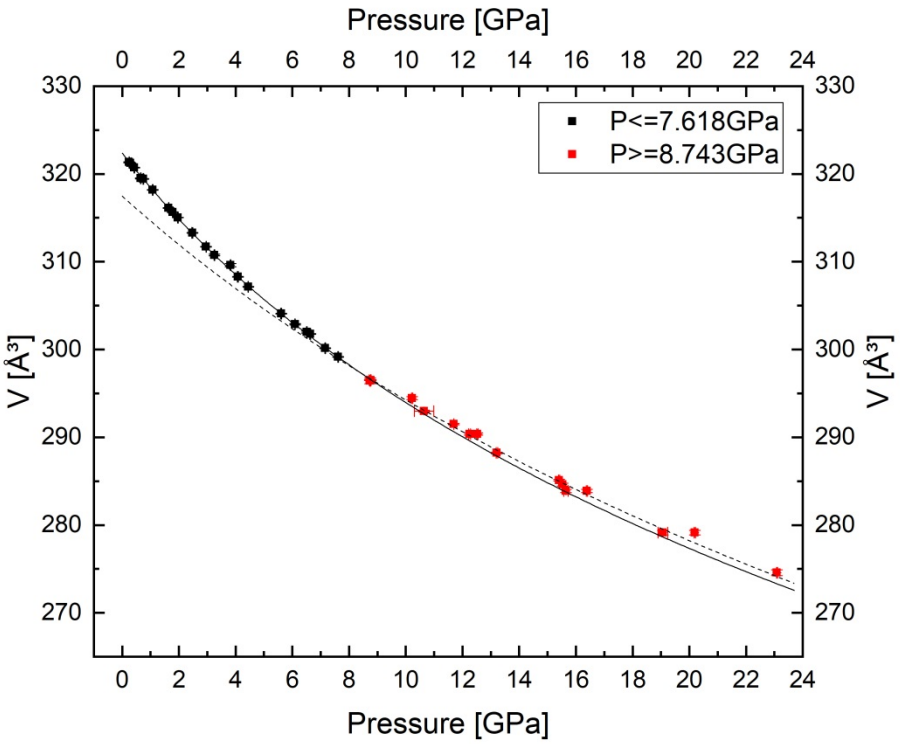

Figure 37 Unit-cell volume of α-$PbAlBO_4$ and both calculated 3rd – order Birch – Murnaghan equations of state. The solid line indicates the equation of state for the first section (V_0 = 322.38(6), K_0 = 77.5(1.2) and *K'* = 7.3(4)) up to 7.62 GPa and the dashed line indicates the equation of state for the second section (V_0 = 317.5(6), K_0 = 109(3) and *K'* = 5) from 8.74 GPa.

To properly compare the 3rd – order Birch – Murnaghan equations of state calculated in this study, Table 7 shows the parameters V_0, K_0 and *K'* as obtained by the EoSFit7_GUI software and also parameters obtained from literature.

	V_0 [Å^3]	K_0 [GPa]	K'	Author
α-PbAlBO$_4$	322.38(6)	77.5(1.2)	7.3(4)	This study
α-PbAlBO$_4$	317(6)	109(3)	5	This study
α-PbAlBO$_4$	321.0(3)	85(5)	5.7(9)	Kalita (2015)
α-PbAlBO$_4$ (DFT)	321.95	77.35	6.51	Gesing et al (2013)
α-PbMnBO$_4$ (DFT)	347.9	52.69	8.4	Gesing et al (2013)
α-PbFeBO$_4$	349.0(4)	73(3)	5.0(9)	Kalita (2015)
α-PbFeBO$_4$	351.23(1)	62.05(1)	-	Murshed et al (2014)
3:2 Mullite	-	172.4	-	Ledbetter et al (1998)
Al$_{6-x}$B$_x$O$_9$	-	190(1)	-	Hoffmann et al (2016)
Al$_5$BO$_9$	656.4(3)	165(7)	4	Gatta et al (2009)
Pb_3O_4 – II	511(1)	20.8(4)	4	Dinnebier et al (2003)
Pb_3O_4 – III	222(2)	98(3)	4	Dinnebier et al (2003)

Table 7 Equation of state parameters for the unit-cell volume of *α-PbAlBO$_4$*.

The first equation of state for *α-PbAlBO$_4$* fitted in this study seems to correlate relatively well with density functional theory (DFT) calculations done by Gesing et al (2013). According to Anderson and Nafe (1965) volume and bulk modulus in oxides are inversely related and the bulk modulus is strongly dependent on the volume. While a doubled volume only halves the bulk modulus in ionic solids, in oxides the bulk modulus is decreased far stronger. This inverse relationship between molar volume and the bulk modulus can be extracted from Table 7. In Pb_3O_4 and in α-$PbAlBO_4$ for example an increase in bulk modulus K_0 can be seen with increasing pressure. In α-$PbAlBO_4$ a second equation of state had to be fitted for the unit-cell volume above 8.743 GPa (see above) while in Pb_3O_4 a phase transition from Pb_3O_4-II to Pb_3O_4-III occurred (Dinnebier et al, 2003).

As mentioned α-$PbAlBO_4$ has the remarkable properties of negative axial compressibility (section 3.1) and uniaxial negative thermal expansion (section 1.1). According to Gogolin et al (2020) these two properties may have a common underlying cause. They propose a mechanism similar in behavior to that of Nuremberg scissors to be one of the reasons for the mentioned properties (Figure 38). While the Al-O bonds act like struts in the mechanical analogy the LEP acts as compression buffer unit.

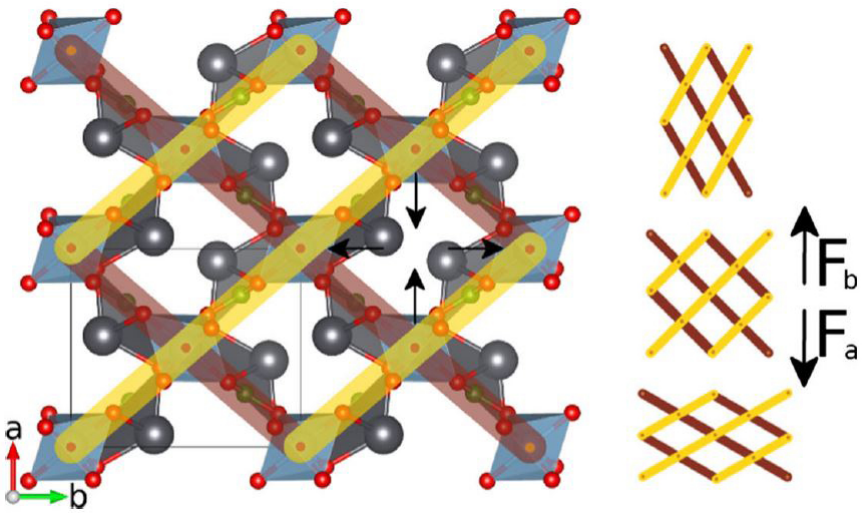

Figure 38 Mechanical scissor analogy, superimposed to the structure in [001], to explain negative axial compressibility and uniaxial negative thermal expansion in α-$PbAlBO_4$ and proposed by Gogolin et al (2020).

5. CONCLUSION

The new gas loading system has been successfully used to load ETH-type DACs, using Böhler-Almax diamond anvils and neon as pressure medium, and is now able to be used for further high pressure loadings using said anvils. Pressures exceeding 10 GPa have been successfully reached and X-ray and Raman measurements were done up to 23 GPa on this first test loading.

The rare property of negative axial compressibility was observed between pressures ranging from 0.2 GPa to about 4 GPa. While equations of state have been fitted to the *a*- and *b*-axis, for the *c*-axis, which experiences negative axial compressibility, a second degree polynomial function has been fitted. Due to a high K' value of K' = 8.6 for the full data set, volume data was truncated between 7.62 and 8.74 GPa which resulted in two equations of state. One of those equations of state also correlates well with density-functional theory calculated values found in the literature (Gesing et al, 2013). *α-PbAlBO₄* behaves according to the relationship of volume and bulk modulus in oxides which was described by Anderson and Nafe (1965), phases with higher volume have a lower bulk modulus and phases with lower volume have a high bulk modulus.

A phase transition as described in the literature (Kalita, 2015) was not observed in the pressure range from 0.2 to just above 23 GPa.

Raman data suggests the presence of different superimposing compression mechanisms, which are compression of the cavity containing the lone electron pair and compression of the structure itself.

6. REFERENCES

Allan D. R.,Miletich R. and Angel R. J. (1996): A diamond anvil cell for single crystal xray diffraction studies to pressures in excess of 10 GPa. Rev. Sci. Instrum. (67), S. 840-842.

Anderson O.L., Nafe J. E.: The Bulk Modulus-Volume Relationship for Oxide Compounds and Related Geophysical Problems. Journal of Geophysical Research 1965 (70), S. 3951–3963.

Angel R. J. (2000): Equations of State. Reviews in Mineralogy and Geochemistry (41), S. 35–59.

Angel R. J. and Finger L. W. (2011): SINGLE: a program to control single-crystal diffractometers. J. Appl. Cryst. (44), S. 247–251.

Anggono J. (2005): Mullite Ceramics: Its Properties, Structure, and Synthesis. Jurnal Teknik Mesin (7)

Baughman R. H., Stafström S., Cui C. and Dantas S. O. (1998): Materials with Negative Compressibilities in One or More Dimensions. Science (279), S. 1522-1524.

Birch F. (1947): Finite Elastic Strain of Cubic Crystals. Phys. Rev. (71), S. 809-824.

Campañá C., Müser M. H., Tse J. S., Herzbach D. and Schöffel P. (2004): Irreversibility of the pressure-induced phase transition of quartz and the relation between three hypothetical post-quartz phases. Phys. Rev. B (70)

Dinnebier R. E., Carlson S., Hanfland M., Jansen M. (2003): Bulk moduli and high-pressure crystal structures of minimum, Pb_3O_4, determined by X-ray powder diffraction. American Mineralogist (88), S. 996–1002.

Evans K. E. and Alderson A. (2000): Auxetic Materials: Functional Materials and Structures from Lateral Thinking! Adv. Mater. (12), S. 617-628

Gatta D. G., Rotiroti N., Fisch M. (2010): Stability at high pressure, elastic behaviour and pressure-induced structural evolution of "Al_5BO_9", a mullite-type ceramic material. Phys. Chem. Minerals (37), S. 227–236.

Gesing Th. M., Mendive C. B., Curti M., Hansmann D., Nénert G., Kalita P. E., Lipinska K. E., Huq A., Cornelius A. L. and Murshed M. M. (2013): Structural properties of mullite-type $Pb(Al_{1-x}Mn_x)BO_4$. Z. Kristallogr. (228), S. 532–543.

Gogolin M., Murshed M. M., Ende M., Miletich R. and Gesing Th. M. (2020): Uniaxial negative thermal expansion in the mullite- and borax-type $PbAlBO_4$ polymorphs. J Mater Sci (55), S. 177–190.

Gonzalez-Platas J., Alvaro M., Nestola F. and Angel R. J. (2016): EosFit7-GUI: a new graphical user interface for equation of state calculations, analyses and teaching. J. Appl. Cryst. (49), S. 1377–1382.

Hoffmann K., Hooper T. J. N., Murshed M. M., Dolotko O., Révay Z., Senyshyn A., Schneider H., Hanna J. V., Gesing Th. M., Fischer R. X. (2016): Formation, stability and crystal structure of mullite-type $Al_{6-x}B_xO_9$. Journal of Solid State Chemistry (243), S. 124–135.

Kalita P. (2015): High Pressure Behaviour of Mullite-Type Oxides: Phase Transitions, Amorphization, Negative Linear Compressibility and Microstructural Implications. PhD Thesis, University of Nevada, Las Vegas, USA.

King Jr. H. E. and Finger L. W. (1979): Diffracted Beam Crystal Centering and Its Application to High-Pressure Crystallography. J. Appl. Cryst. (12), S. 374–378.

Kingma K. J., Hemley R. J., Mao H. K. and Veblen D. R. (1993): New High-Pressure Transformation in alpha-Quartz. Physical Review Letters (70), S. 3927-3930

Kriegesmann J. and Kratz N. (2015): Definition, Systematik und Geschichte der Keramik: Von der Tonkeramik bis zur Hochleistungskeramik. Keram. Z. (3), S. 152–157.

Ledbetter H., Kim S., Balzar D. (1998): Elastic Properties of Mullite. J. Am. Ceram. Soc. (81), S. 1025–1028.

Mao H. K., Xu J. and Bell P. M. (1986): Calibration of the Ruby Pressure Gauge to 800 kbar Under Quasi-Hydrostatic Conditions. Journal of Geophysical Research (91), S. 4673–4676.

Miletich R., Allan D. R. and Kuhs W. F.: High-Pressure Single-Crystal Techniques. Reviews in Mineralogy and Geochemistry (41), S. 445–519.

Momma K. and Izumi F. (2011): VESTA 3 for three-dimensional visualization of crystal, volumetric and morphology data. J. Appl. Cryst. (44), S. 1272–1276.

Murshed M. M., Mendive C. B., Curti M., Nénert G., Kalita P., Lipinska K., Cornelius A. L., Huq A., Gesing Th. M. (2014): Anisotropic lattice thermal expansion of $PbFeBO_4$: A study by X-Ray and neutron diffraction, Raman spectroscopy and DFT calculations. Materials Research Bulletin (59), S. 170–178.

Park H., Barbier J. and Hammond R. P. (2003): Crystal structure and polymorphism of $PbAlBO_4$. Solid State Sciences (5), S. 565–571.

Richet P. and Gillet P. (1997): Pressure-induced amorphization of minerals: a review. Eur. J. Mineral (9), S. 907–933.

Scheidl. K. S., Kurnosov A., Trots D. M., Ballaran T. B., Angel R. J., Miletich R. (2016): Extending the single-crystal quartz pressure gauge up to hydrostatic pressure of 19 GPa. J. Appl. Cryst. (49), S. 2129–2137.

Schneider H., Fischer R. X., Gesing Th. M., Schreuer J., Mühlberg M. (2012): Crystal chemistry and properties of mullite-type $Bi_2M_4O_9$: An overview. Int. J. Mat. Res. (103), S. 422–429.

Stoe & Cie (2002). X-Area. Stoe & Cie, Darmstadt, Germany

Sugano S. and Tanabe Y. (1958): Absorption Spectra of Cr^{3+} in Al_2O_3 Part A. Theoretical Studies of the Absorption Bands and Lines. J. Phys. Soc. Jpn. (13), S. 880–899.

7. TABLE OF TABLES

8. TABLE OF FIGURES

9. TABLE OF EQUATIONS

10. ADDENDUM

In this section the peak fitting results of the Raman bands and waterfall plots of all measured Raman spectra for each orientation are presented. “SE” refers to the standard error as calculated by the PeakFit software, while “FWHM” stands for full width at half maximum. As in section 3.1, pressure is calculated by unit-cell volume of quartz or by ruby luminescence. “M1” “M2” and “M3” refer to the DACs orientation as explained in section 3.2.

M1

Pressure (GPa)	v1 (cm^{-1})	SE v1	FWHM v1	SE FWHM v1	v2 (cm^{-1})	SE v2	FWHM v2	SE FWHM v2	v3 (cm^{-1})	SE v3	FWHM v3	SE FWHM v3
8.83(2)	54.680	0.022	1.44	0.09	82.095	0.012	1.75	0.04	128.662	0.004	1.94	0.02
12.56(4)	57.016	0.019	1.22	0.08	84.326	0.014	2.09	0.04	129.140	0.007	4.96	0.03
16.39(8)	60.257	0.057	1.23	0.20	87.194	0.017	2.74	0.05	126.328	0.013	6.82	0.05
20.45(17)	63.557	0.173	2.06	0.51	90.128	0.014	2.59	0.04	125.775	0.016	7.79	0.05
15.53(3)	59.731	0.047	1.23	0.20	86.972	0.007	1.79	0.02	127.347	0.012	5.02	0.05
10.22(2)	55.649	0.021	1.13	0.09	83.348	0.008	1.76	0.03	130.213	0.004	2.56	0.01
10.65(34)	55.942	0.022	1.22	0.09	83.627	0.009	1.80	0.03	130.327	0.005	3.09	0.02
11.69(2)	56.459	0.018	1.18	0.07	84.105	0.006	1.75	0.02	130.176	0.005	3.84	0.02
13.21(3)	57.929	0.033	1.33	0.13	85.181	0.007	1.74	0.02	128.552	0.009	4.93	0.04
15.41(3)	59.713	0.061	1.52	0.25	86.467	0.009	1.85	0.03	126.767	0.013	4.96	0.05
0.37(2)	54.881	0.010	1.23	0.04	79.957	0.002	1.36	0.01	107.780	0.002	1.54	0.01
0.79(2)	54.610	0.228	1.22	0.92					109.109	0.046	1.55	0.16
1.38(2)	54.314	0.335	1.35	1.35								
1.92(2)	54.157	0.017	1.39	0.07	80.032	0.002	1.43	0.01	112.615	0.003	1.61	0.01
2.46(2)	53.992	0.033	2.19	0.13	80.143	0.004	1.49	0.01	114.400	0.005	1.67	0.02
2.81(2)	53.900	0.016	1.32	0.06	80.178	0.002	1.45	0.01	115.680	0.003	1.63	0.01
2.96(2)	53.807	0.015	1.32	0.06	80.091	0.002	1.48	0.01	115.772	0.003	1.65	0.01
3.16(2)	53.795	0.015	1.32	0.06	80.153	0.002	1.46	0.01	116.324	0.003	1.60	0.01
3.54(2)	53.724	0.016	1.39	0.06	80.224	0.002	1.54	0.01	117.604	0.003	1.68	0.01
4.23(2)	53.649	0.387	1.52	1.57					119.392	0.062	1.74	0.21
4.54(2)	53.597	0.010	1.43	0.04								
5.11(2)	53.613	0.322	1.43	1.31					121.509	0.054	1.71	0.19
5.42(2)	53.615	0.007	1.35	0.03								
6.21(2)	53.640	0.012	1.57	0.05								
6.95(2)	53.792	0.007	1.41	0.03								
7.29(2)	54.018	0.008	1.37	0.03								
7.86(2)	54.050	0.009	1.49	0.04								
8.33(2)	54.291	0.007	1.43	0.02								
8.94(2)	54.529	0.009	1.43	0.03								
10.07(2)	56.524	0.082	2.30	0.33					119.139	0.072	9.36	0.21

M1

Pressure (GPa)	v4 (cm^{-1})	SE v4	FWHM v4	SE FWHM v4	v5 (cm^{-1})	SE v5	FWHM v5	SE FWHM v5	v6 (cm^{-1})	SE v6	FWHM v6	SE FWHM v6
8.83(2)	144.275	0.039	7.48	0.14	230.381	0.200	6.54	0.81	460.654	0.042	9.53	0.17
12.56(4)	143.108	0.065	4.34	0.24	229.863	0.104	6.56	0.42	473.046	0.023	8.89	0.10
16.39(8)	146.899	0.034	3.31	0.12	230.279	0.086	5.39	0.32	483.553	0.045	8.98	0.18
20.45(17)	151.465	0.026	3.67	0.08	232.007	0.045	6.12	0.18	491.494	0.018	7.99	0.07
15.53(3)	145.909	0.020	3.27	0.08	230.672	0.027	5.70	0.10	481.773	0.022	8.45	0.09
10.22(2)	143.239	0.043	6.23	0.14	230.380	0.032	6.56	0.13	465.775	0.021	8.82	0.08
10.65(34)	142.848	0.046	5.53	0.15	230.099	0.064	7.23	0.26	467.699	0.026	8.77	0.10
11.69(2)	142.576	0.041	4.92	0.14	230.306	0.064	5.85	0.19	470.179	0.022	8.77	0.08
13.21(3)	143.270	0.039	3.72	0.15	230.171	0.046	6.56	0.19	475.769	0.026	8.61	0.10
15.41(3)	145.698	0.024	3.38	0.10	230.580	0.101	6.27	0.41	480.773	0.026	8.69	0.10
0.37(2)	172.229	0.044	6.40	0.16	229.707	0.046	4.18	0.16	425.652	0.098	12.21	0.40
0.79(2)	170.770	0.948	6.64	3.54	229.740	0.037	4.17	0.14	427.578	0.070	10.79	0.29
1.38(2)	168.681	1.344	7.29	5.45	229.941	0.033	4.28	0.12	430.403	0.074	9.68	0.27
1.92(2)	166.955	0.072	7.46	0.25	230.238	0.046	4.63	0.15	432.903	0.092	10.43	0.37
2.46(2)	165.023	0.120	8.06	0.46	230.409	0.049	4.60	0.13	435.575	0.103	9.69	0.29
2.81(2)	163.257	0.075	8.74	0.25	230.422	0.033	4.57	0.12	437.444	0.071	9.39	0.29
2.96(2)	162.948	0.076	9.08	0.23	230.349	0.036	4.73	0.13	437.630	0.074	9.71	0.24
3.16(2)	162.188	0.079	9.47	0.24	230.427	0.031	4.52	0.12	438.448	0.065	9.82	0.26
3.54(2)	160.500	0.085	10.15	0.25	230.500	0.031	4.68	0.11	440.599	0.061	9.32	0.21
4.23(2)	157.815	1.905	9.65	6.88	230.496	0.032	4.71	0.13	443.540	0.069	9.88	0.22
4.54(2)	156.628	0.052	9.87	0.17	230.498	0.034	5.11	0.14	444.617	0.069	9.46	0.23
5.11(2)	154.534	1.756	8.70	6.42	230.498	0.031	5.04	0.12	446.993	0.067	9.63	0.20
5.42(2)	153.197	0.043	9.04	0.15	230.466	0.020	5.07	0.08	448.474	0.039	9.39	0.12
6.21(2)	150.371	0.065	9.11	0.22	230.278	0.023	5.77	0.09	451.571	0.043	9.21	0.15
6.95(2)	148.214	0.045	8.64	0.15	230.144	0.018	5.76	0.07	454.165	0.030	9.19	0.11
7.29(2)	147.226	0.053	8.19	0.19	230.245	0.020	5.68	0.08	455.684	0.034	9.14	0.12
7.86(2)	145.807	0.065	7.87	0.24	230.076	0.021	5.94	0.08	457.586	0.036	9.21	0.13
8.33(2)	144.811	0.056	7.59	0.21	230.045	0.016	5.88	0.06	459.204	0.025	8.97	0.09
8.94(2)	143.432	0.103	8.15	0.32	229.896	0.019	5.91	0.07	461.602	0.030	8.78	0.11
10.07(2)	141.471	0.028	4.07	0.05	227.420	0.013	6.45	0.05	468.471	0.035	9.32	0.12

M1

Pressure (GPa)	v7 (cm^{-1})	SE v7	FWHM v7	SE FWHM v7	v8 (cm^{-1})	SE v8	FWHM v8	SE FWHM v8	v9 (cm^{-1})	SE v9	FWHM v9	SE FWHM v9
8.83(2)	551.930	0.143	17.40	0.58	714.920	0.133	7.93	0.54	1003.113	0.099	11.67	0.33
12.56(4)	559.813	0.093	15.34	0.38	718.717	0.098	6.08	0.40	1016.482	0.073	12.88	0.26
16.39(8)	566.480	0.224	27.47	0.91	726.333	0.287	7.00	1.16	1029.221	0.168	16.20	0.59
20.45(17)	573.021	0.077	14.17	0.31	733.146	0.200	7.58	0.81	1038.451	0.069	16.44	0.26
15.53(3)	566.445	0.074	12.03	0.30	724.568	0.082	5.63	0.33	1027.367	0.071	13.84	0.27
10.22(2)	555.959	0.062	10.92	0.25	716.219	0.068	6.37	0.28	1008.612	0.051	11.93	0.20
10.65(34)	557.354	0.079	11.04	0.32	716.882	0.086	5.76	0.35	1010.803	0.069	12.52	0.24
11.69(2)	558.856	0.066	10.16	0.27	717.819	0.078	6.25	0.32	1013.325	0.061	12.86	0.23
13.21(3)	562.196	0.096	11.55	0.39	720.462	0.115	6.35	0.47	1019.203	0.077	12.11	0.29
15.41(3)	565.607	0.097	11.19	0.39	723.562	0.138	7.69	0.56	1025.032	0.080	13.92	0.30
0.37(2)	534.334	0.190	10.04	0.77	714.369	0.046	5.89	0.19	969.192	0.065	6.56	0.26
0.79(2)	535.511	0.167	10.38	0.59	714.300	0.039	5.84	0.16	971.281	0.051	5.89	0.19
1.38(2)	536.778	0.169	9.09	0.46	714.083	0.053	7.15	0.21	973.768	0.050	6.06	0.18
1.92(2)	538.220	0.195	7.79	0.79	714.046	0.069	6.24	0.28	975.982	0.070	5.95	0.28
2.46(2)	539.415	0.264	7.20	0.73	713.897	0.091	7.60	0.37	978.625	0.082	6.05	0.31
2.81(2)	540.279	0.171	8.96	0.53	713.954	0.061	6.33	0.25	980.385	0.062	6.43	0.24
2.96(2)	540.645	0.188	8.11	0.52	713.945	0.067	6.86	0.27	980.544	0.064	6.83	0.21
3.16(2)	540.845	0.159	8.84	0.64	713.871	0.068	7.52	0.28	981.377	0.058	6.73	0.22
3.54(2)	541.715	0.198	9.44	0.54	714.004	0.063	7.03	0.25	983.259	0.058	6.65	0.21
4.23(2)	543.535	0.199	8.63	0.54	714.101	0.081	7.59	0.33	985.926	0.067	7.12	0.25
4.54(2)	544.073	0.188	8.68	0.65	713.885	0.086	7.01	0.35	986.975	0.073	7.67	0.26
5.11(2)	545.429	0.167	9.53	0.68	713.672	0.081	6.69	0.33	989.235	0.072	7.51	0.27
5.42(2)	546.202	0.116	9.03	0.42	713.714	0.047	6.60	0.19	990.778	0.046	7.83	0.18
6.21(2)	547.646	0.149	12.37	0.60	713.559	0.063	7.00	0.26	993.832	0.059	8.54	0.20
6.95(2)	549.209	0.100	10.35	0.41	713.594	0.044	6.87	0.18	996.403	0.044	8.97	0.16
7.29(2)	549.922	0.118	9.82	0.48	713.789	0.049	7.08	0.20	997.852	0.050	9.13	0.19
7.86(2)	551.063	0.138	11.77	0.56	713.864	0.057	7.26	0.23	999.700	0.061	9.70	0.21
8.33(2)	551.985	0.099	10.37	0.40	714.079	0.039	6.64	0.16	1001.371	0.045	10.08	0.17
8.94(2)	553.625	0.112	9.72	0.45	714.478	0.042	6.23	0.17	1003.845	0.063	11.27	0.23
10.07(2)	554.485	0.254	14.47	1.03	710.609	0.083	8.72	0.33	1003.383	0.066	12.34	0.24

M2

Pressure (GPa)	v1 (cm^{-1})	SE v1	FWHM v1	SE FWHM v1	v2 (cm^{-1})	SE v2	FWHM v2	SE FWHM v2	v3 (cm^{-1})	SE v3	FWHM v3	SE FWHM v3
8.83(2)	54.661	0.028	1.55	0.11	82.009	0.004	1.60	0.01				
12.56(4)	57.094	0.069	1.42	0.28	84.432	0.008	2.08	0.02	129.871	0.014	5.26	0.05
16.39(8)	60.506	0.132	1.68	0.36	87.328	0.010	2.62	0.03	127.070	0.035	7.20	0.13
20.45(17)	63.546	0.179	2.09	0.49	90.186	0.008	2.70	0.02	126.344	0.035	7.99	0.11
15.53(3)	59.863	0.070	1.23	0.21	87.000	0.005	1.67	0.02	127.382	0.019	4.96	0.08
10.22(2)	55.672	0.018	1.20	0.07	83.276	0.002	1.62	0.01	130.262	0.002	2.66	0.01
10.65(34)	55.846	0.027	1.28	0.11	83.554	0.003	1.82	0.01	130.414	0.004	3.19	0.01
11.69(2)	56.545	0.034	1.12	0.12	84.137	0.003	1.54	0.01	130.452	0.007	3.93	0.02
13.21(3)	57.924	0.061	1.07	0.23	85.243	0.005	1.62	0.02	128.952	0.018	4.97	0.07
15.41(3)	59.716	0.059	1.48	0.24	86.467	0.009	1.85	0.03	126.766	0.013	4.96	0.05
0.37(2)	54.704	0.011	1.37	0.04	79.747	0.003	1.47	0.01	107.581	0.005	1.66	0.02
0.79(2)	54.559	0.007	1.37	0.03					109.061	0.003	1.66	0.01
1.38(2)	54.287	0.008	1.41	0.03					111.019	0.003	1.70	0.01
1.92(2)	54.123	0.015	1.40	0.06	80.016	0.003	1.43	0.01	112.615	0.005	1.64	0.02
2.46(2)	53.912	0.010	1.41	0.04					114.284	0.003	1.73	0.01
2.81(2)	53.797	0.018	1.49	0.07	80.068	0.003	1.63	0.01	115.584	0.004	1.81	0.01
2.96(2)	53.795	0.018	1.44	0.07	80.090	0.003	1.63	0.01	115.768	0.004	1.77	0.01
3.16(2)	53.629	0.014	1.47	0.05	79.998	0.002	1.60	0.01	116.209	0.003	1.75	0.01
3.54(2)	53.661	0.017	1.54	0.06	80.178	0.002	1.68	0.01	117.568	0.003	1.80	0.01
4.23(2)	53.596	0.015	1.63	0.06					119.344	0.003	1.86	0.01
4.54(2)	53.545	0.019	1.75	0.08					120.098	0.003	1.81	0.01
5.11(2)	53.582	0.011	1.47	0.04								
5.42(2)	53.606	0.007	1.43	0.03								
6.21(2)	53.594	0.009	1.46	0.04								
6.95(2)	53.806	0.015	1.63	0.06								
7.29(2)	53.938	0.017	1.66	0.07								
7.86(2)	54.047	0.008	1.43	0.03								
8.33(2)	54.155	0.009	1.56	0.03								
8.94(2)	54.462	0.010	1.45	0.04								
10.07(2)	56.681	0.095	2.33	0.38					118.914	0.054	9.52	0.19

M2

Pressure (GPa)	v7 (cm^{-1})	SE v7	FWHM v7	SE FWHM v7	v8 (cm^{-1})	SE v8	FWHM v8	SE FWHM v8	v9 (cm^{-1})	SE v9	FWHM v9	SE FWHM v9
8.83(2)	552.936	0.187	19.67	0.76	714.496	0.155	7.29	0.63	1003.173	0.152	11.24	0.48
12.56(4)	560.722	0.087	9.89	0.35	718.761	0.095	6.29	0.39	1016.648	0.069	12.92	0.25
16.39(8)	568.011	0.070	11.32	0.25	726.808	0.238	12.61	0.97	1030.059	0.075	18.49	0.23
20.45(17)	573.453	0.057	12.62	0.18	733.273	0.365	15.59	1.47	1038.326	0.057	16.83	0.18
15.53(3)	566.460	0.068	10.63	0.27	724.474	0.079	5.53	0.32	1027.227	0.062	14.03	0.25
10.22(2)	556.124	0.086	10.06	0.35	715.956	0.063	6.25	0.25	1008.429	0.062	12.21	0.21
10.65(34)	557.620	0.135	13.72	0.55	716.705	0.097	5.93	0.39	1010.514	0.087	12.72	0.33
11.69(2)	559.115	0.072	9.49	0.25	717.735	0.058	6.02	0.23	1013.367	0.054	12.45	0.20
13.21(3)	562.568	0.070	9.99	0.28	720.353	0.080	5.29	0.32	1019.275	0.057	12.59	0.21
15.41(3)	565.606	0.098	11.21	0.39	723.563	0.139	7.68	0.56	1025.024	0.081	13.93	0.30
0.37(2)	534.133	0.152	9.57	0.62	714.396	0.058	5.65	0.24	969.141	0.038	5.91	0.14
0.79(2)	534.937	0.133	10.71	0.41	714.263	0.045	6.69	0.18	971.103	0.030	6.24	0.12
1.38(2)	536.220	0.132	10.39	0.36	714.164	0.051	7.60	0.21	973.861	0.031	5.88	0.12
1.92(2)	537.625	0.233	9.71	0.64	714.090	0.082	7.50	0.33	976.072	0.056	6.05	0.21
2.46(2)	538.997	0.138	9.62	0.38	713.899	0.050	6.52	0.20	978.497	0.039	6.31	0.15
2.81(2)	540.006	0.183	8.56	0.50	713.902	0.075	7.29	0.30	980.225	0.053	6.40	0.21
2.96(2)	539.871	0.182	9.80	0.50	713.967	0.068	7.09	0.28	980.494	0.052	6.67	0.20
3.16(2)	540.647	0.213	9.35	0.58	713.891	0.074	6.77	0.29	981.301	0.058	6.74	0.22
3.54(2)	541.910	0.197	7.85	0.54	713.994	0.084	6.92	0.34	983.128	0.068	6.93	0.26
4.23(2)	543.342	0.148	8.16	0.53	714.010	0.077	6.93	0.31	985.863	0.064	7.39	0.26
4.54(2)	544.393	0.228	7.17	0.63	713.787	0.093	7.26	0.38	987.041	0.085	7.81	0.24
5.11(2)	545.382	0.157	8.84	0.54	713.744	0.073	6.82	0.30	989.239	0.066	7.72	0.24
5.42(2)	546.319	0.142	8.88	0.57	713.646	0.063	6.54	0.25	990.736	0.063	7.94	0.23
6.21(2)	547.764	0.119	9.16	0.48	713.563	0.049	7.10	0.20	993.787	0.054	8.52	0.19
6.95(2)	549.341	0.174	9.34	0.48	713.841	0.108	9.07	0.44	996.447	0.090	8.84	0.31
7.29(2)	550.272	0.136	9.72	0.55	713.748	0.068	7.62	0.28	997.797	0.069	9.59	0.22
7.86(2)	551.271	0.080	9.65	0.32	713.846	0.037	6.25	0.15	999.736	0.046	9.87	0.17
8.33(2)	552.279	0.103	10.22	0.42	714.022	0.055	6.62	0.22	1001.362	0.072	10.33	0.26
8.94(2)	553.588	0.094	9.59	0.38	714.361	0.051	6.96	0.21	1003.679	0.059	11.13	0.22
10.07(2)	554.409	0.224	11.31	0.91	710.946	0.087	7.83	0.35	1003.962	0.071	13.10	0.24

M2

Pressure (GPa)	v4 (cm^{-1})	SE v4	FWHM v4	SE FWHM v4	v5 (cm^{-1})	SE v5	FWHM v5	SE FWHM v5	v6 (cm^{-1})	SE v6	FWHM v6	SE FWHM v6
8.83(2)					230.314	0.122	8.83	0.49	460.681	0.088	9.84	0.36
12.56(4)	141.817	0.032	4.56	0.11	230.070	0.019	5.99	0.08	473.180	0.031	8.57	0.12
16.39(8)	147.152	0.013	3.47	0.05	230.694	0.012	5.87	0.05	484.342	0.026	8.11	0.10
20.45(17)	151.387	0.010	3.72	0.04	231.985	0.016	5.76	0.06	491.607	0.022	7.91	0.08
15.53(3)	146.018	0.015	3.29	0.06	230.711	0.013	5.74	0.05	481.814	0.022	8.14	0.08
10.22(2)	142.451	0.098	6.13	0.35	230.399	0.017	6.00	0.07	465.740	0.028	8.78	0.10
10.65(34)	140.750	0.139	7.89	0.36	230.145	0.023	6.26	0.09	467.607	0.042	8.99	0.14
11.69(2)	140.283	0.100	7.92	0.25	230.275	0.017	5.99	0.07	470.381	0.024	8.74	0.09
13.21(3)	143.042	0.028	3.88	0.11	230.287	0.015	5.93	0.06	475.904	0.027	8.68	0.10
15.41(3)	145.697	0.023	3.37	0.09	230.533	0.044	5.57	0.16	480.772	0.027	8.69	0.10
0.37(2)	172.059	0.025	6.22	0.09	229.538	0.058	4.64	0.17	425.656	0.068	9.64	0.28
0.79(2)	170.688	0.019	6.69	0.07	229.669	0.032	4.20	0.12	427.641	0.053	10.52	0.21
1.38(2)	168.650	0.022	7.00	0.08	229.990	0.030	4.24	0.12	430.569	0.049	9.96	0.20
1.92(2)	166.914	0.049	7.23	0.18	230.127	0.048	4.58	0.14	433.051	0.084	11.47	0.34
2.46(2)	164.821	0.036	7.83	0.13	230.175	0.029	4.70	0.10	435.510	0.048	9.28	0.19
2.81(2)	163.084	0.069	8.92	0.22	230.243	0.039	4.62	0.14	437.481	0.064	9.04	0.23
2.96(2)	162.876	0.071	9.12	0.22	230.350	0.035	4.62	0.13	437.800	0.059	9.74	0.19
3.16(2)	162.001	0.056	9.35	0.18	230.174	0.039	4.77	0.14	438.509	0.067	9.59	0.25
3.54(2)	160.326	0.071	10.21	0.20	230.425	0.040	4.75	0.14	440.508	0.072	9.48	0.24
4.23(2)	157.763	0.070	10.23	0.20	230.447	0.031	4.83	0.11	443.421	0.060	9.08	0.20
4.54(2)	156.616	0.090	10.31	0.26	230.440	0.040	4.86	0.14	444.708	0.076	9.22	0.21
5.11(2)	154.547	0.058	9.42	0.18	230.497	0.028	5.02	0.11	446.991	0.057	9.52	0.16
5.42(2)	153.162	0.039	9.12	0.13	230.442	0.025	5.27	0.10	448.466	0.053	9.82	0.15
6.21(2)	150.285	0.054	8.93	0.18	230.217	0.021	5.53	0.08	451.501	0.040	9.52	0.13
6.95(2)	148.261	0.089	8.43	0.33	230.300	0.031	5.57	0.12	454.184	0.061	9.22	0.17
7.29(2)	147.230	0.110	7.91	0.40	230.166	0.023	5.73	0.08	455.595	0.045	9.53	0.14
7.86(2)	145.868	0.062	7.78	0.24	230.022	0.013	5.88	0.05	457.518	0.027	9.23	0.09
8.33(2)	144.663	0.074	8.05	0.26	229.935	0.019	5.92	0.07	459.097	0.039	9.00	0.14
8.94(2)	142.722	0.133	10.01	0.52	229.807	0.015	5.94	0.06	461.488	0.030	8.86	0.10
10.07(2)	141.656	0.015	3.99	0.06	227.422	0.013	6.12	0.05	468.679	0.036	9.48	0.12

M3

Pressure (GPa)	v1 (cm^{-1})	SE v1	FWHM v1	SE FWHM v1	v2 (cm^{-1})	SE v2	FWHM v2	SE FWHM v2	v3 (cm^{-1})	SE v3	FWHM v3	SE FWHM v3
8.83(2)	54.606	0.030	1.61	0.12	81.982	0.005	1.53	0.02	128.621	0.003	1.93	0.01
12.56(4)	56.979	0.044	1.36	0.18	84.387	0.006	1.94	0.02	129.244	0.014	5.02	0.05
16.39(8)	60.402	0.099	1.47	0.29	87.089	0.013	2.83	0.04	126.643	0.027	7.32	0.09
20.45(17)	63.678	0.171	1.97	0.47	90.165	0.009	2.69	0.03	126.050	0.027	8.04	0.09
15.53(3)	59.747	0.071	1.16	0.22	87.002	0.006	1.84	0.02	127.570	0.021	5.19	0.08
10.22(2)	55.559	0.036	1.15	0.14	83.245	0.004	1.66	0.01	130.233	0.004	2.57	0.01
10.65(34)	55.837	0.036	1.18	0.14	83.482	0.004	1.74	0.01	130.357	0.006	3.55	0.02
11.69(2)	56.546	0.034	1.14	0.12	84.126	0.004	1.65	0.01	130.464	0.007	3.93	0.02
13.21(3)	57.978	0.056	1.11	0.21	85.347	0.005	1.65	0.02	129.087	0.016	4.95	0.06
15.41(3)	59.724	0.061	1.11	0.24	86.751	0.005	1.70	0.02	127.494	0.017	4.94	0.07
0.37(2)	54.645	0.010	1.43	0.04	79.689	0.004	1.56	0.01				
0.79(2)	54.563	0.009	1.19	0.03	79.856	0.003	1.34	0.01				
1.38(2)	54.352	0.012	1.37	0.04	79.976	0.003	1.50	0.01				
1.92(2)	54.007	0.012	1.39	0.05	79.879	0.003	1.50	0.01				
2.46(2)	53.938	0.019	1.61	0.07	80.043	0.004	1.68	0.01				
2.81(2)	53.780	0.015	1.35	0.06	80.034	0.003	1.53	0.01				
2.96(2)	53.751	0.016	1.41	0.07	80.025	0.003	1.52	0.01				
3.16(2)	53.795	0.017	1.46	0.07	80.139	0.003	1.58	0.01				
3.54(2)	53.679	0.021	1.61	0.08	80.172	0.003	1.69	0.01				
4.23(2)	53.593	0.023	1.58	0.09	80.263	0.003	1.73	0.01				
4.54(2)	53.577	0.012	1.53	0.05								
5.11(2)	53.556	0.017	1.68	0.07								
5.42(2)	53.622	0.024	1.69	0.10	80.571	0.002	1.73	0.01				
6.21(2)	53.706	0.027	1.61	0.11	80.793	0.002	1.70	0.01				
6.95(2)	53.786	0.020	1.56	0.08								
7.29(2)	53.906	0.017	1.57	0.07								
7.86(2)	54.078	0.019	1.59	0.08								
8.33(2)	54.238	0.018	1.51	0.07								
8.94(2)	54.509	0.030	1.64	0.12								
10.07(2)	56.551	0.295	4.86	1.20					119.720	0.053	9.87	0.20

M3

Pressure (GPa)	v4 (cm^{-1})	SE v4	FWHM v4	SE FWHM v4	v5 (cm^{-1})	SE v5	FWHM v5	SE FWHM v5	v6 (cm^{-1})	SE v6	FWHM v6	SE FWHM v6
8.83(2)	144.266	0.079	7.59	0.28	230.272	0.063	6.86	0.26	460.661	0.052	9.04	0.19
12.56(4)	141.812	0.050	4.45	0.17	229.879	0.088	6.02	0.36				
16.39(8)	146.986	0.013	3.28	0.05	230.469	0.041	5.93	0.14	483.785	0.045	7.52	0.18
20.45(17)	151.504	0.010	3.60	0.04	232.024	0.018	5.85	0.07	491.550	0.023	7.66	0.09
15.53(3)	145.893	0.016	3.33	0.06	230.682	0.015	5.94	0.06	481.717	0.025	8.36	0.09
10.22(2)					230.353	0.016	6.13	0.06	465.681	0.026	8.73	0.10
10.65(34)	139.914	0.198	9.15	0.48	230.129	0.024	6.07	0.09	467.694	0.028	8.80	0.10
11.69(2)	140.667	0.078	7.45	0.20	230.338	0.019	5.91	0.07	470.321	0.024	8.61	0.09
13.21(3)	143.129	0.028	3.83	0.11	230.366	0.018	5.87	0.07	475.856	0.025	8.71	0.09
15.41(3)	145.756	0.014	3.31	0.06	230.713	0.016	5.73	0.06	481.211	0.023	8.51	0.09
0.37(2)	172.086	0.055	6.43	0.20	229.500	0.152	4.44	0.44	425.652	0.146	13.27	0.59
0.79(2)	170.765	0.061	6.89	0.21	229.825	0.089	4.52	0.28	427.636	0.100	12.16	0.41
1.38(2)	168.741	0.068	7.28	0.25	230.011	0.105	4.34	0.34	429.997	0.153	18.93	0.62
1.92(2)	166.862	0.069	7.35	0.24	230.077	0.084	4.93	0.30	432.564	0.098	12.46	0.40
2.46(2)	164.908	0.094	7.90	0.32	230.262	0.103	4.90	0.33	435.409	0.142	15.51	0.58
2.81(2)	163.222	0.092	8.45	0.29	230.241	0.070	4.91	0.22	437.317	0.084	10.64	0.34
2.96(2)	162.942	0.101	8.69	0.30	230.264	0.073	4.17	0.29	437.629	0.086	9.62	0.35
3.16(2)	162.308	0.101	8.98	0.30	230.488	0.077	4.69	0.26	438.590	0.085	9.68	0.30
3.54(2)	160.484	0.119	9.52	0.34	230.435	0.071	5.08	0.20	440.373	0.090	9.71	0.26
4.23(2)	157.842	0.136	9.91	0.39	230.452	0.059	5.36	0.17	443.329	0.076	9.95	0.21
4.54(2)	156.730	0.077	9.61	0.24	230.412	0.055	5.18	0.16	444.647	0.074	9.44	0.20
5.11(2)	154.712	0.098	9.08	0.29	230.472	0.050	5.10	0.19	446.900	0.074	9.59	0.20
5.42(2)	153.366	0.146	8.78	0.43	230.441	0.050	5.63	0.18	448.358	0.065	8.99	0.20
6.21(2)	150.664	0.204	8.71	0.59	230.292	0.040	5.54	0.14	451.515	0.055	9.39	0.17
6.95(2)	148.370	0.200	8.16	0.75	230.136	0.039	5.78	0.14	454.191	0.053	9.73	0.17
7.29(2)	147.169	0.189	9.34	0.77	230.101	0.032	5.85	0.12	455.663	0.047	9.33	0.18
7.86(2)	145.247	0.333	12.37	1.01	230.062	0.029	6.04	0.10	457.521	0.044	9.33	0.15
8.33(2)	143.410	0.718	12.74	1.93	229.960	0.028	5.92	0.10	459.190	0.039	8.97	0.15
8.94(2)					229.801	0.026	6.05	0.09	461.469	0.037	8.89	0.13
10.07(2)					227.450	0.017	6.52	0.06	468.565	0.033	8.74	0.12

M3

Pressure (GPa)	v7 (cm^{-1})	SE v7	FWHM v7	SE FWHM v7	v8 (cm^{-1})	SE v8	FWHM v8	SE FWHM v8	v9 (cm^{-1})	SE v9	FWHM v9	SE FWHM v9
8.83(2)	552.630	0.142	12.99	0.58	714.475	0.102	6.06	0.41	1002.916	0.106	10.91	0.35
12.56(4)												
16.39(8)	567.311	0.141	15.77	0.57					1029.296	0.143	15.85	0.52
20.45(17)	573.316	0.069	12.69	0.24					1038.299	0.071	16.72	0.25
15.53(3)	566.428	0.077	11.46	0.31	725.005	0.203	14.02	0.82	1027.208	0.065	13.91	0.26
10.22(2)	556.318	0.075	9.42	0.30	715.944	0.051	6.06	0.21	1008.490	0.055	12.19	0.21
10.65(34)	557.505	0.084	9.63	0.33	716.572	0.061	6.22	0.25	1010.527	0.064	12.87	0.23
11.69(2)	559.055	0.070	9.59	0.27	717.631	0.055	5.45	0.22	1013.316	0.053	12.59	0.20
13.21(3)	562.634	0.067	10.43	0.27	720.542	0.086	5.14	0.35	1019.654	0.062	12.59	0.24
15.41(3)	566.146	0.068	10.57	0.24	723.951	0.133	8.29	0.54	1026.127	0.058	13.89	0.21
0.37(2)	534.190	0.476	9.95	1.39	714.365	0.055	5.58	0.21	969.093	0.113	5.68	0.41
0.79(2)	534.989	0.294	11.14	0.81	714.312	0.043	6.08	0.17	971.108	0.080	5.85	0.28
1.38(2)	536.696	0.345	9.90	0.95	714.295	0.059	6.84	0.24	973.837	0.109	6.19	0.35
1.92(2)	537.322	0.298	9.99	0.97	714.098	0.056	7.02	0.23	975.910	0.077	5.80	0.28
2.46(2)					714.014	0.088	8.12	0.36	978.349	0.115	6.72	0.35
2.81(2)	540.171	0.271	9.79	0.77	713.913	0.055	6.66	0.22	980.314	0.083	7.48	0.26
2.96(2)	540.325	0.327	7.81	0.90	713.801	0.064	6.49	0.26	980.546	0.084	6.17	0.32
3.16(2)	540.863	0.338	7.69	0.93	713.752	0.063	6.31	0.26	981.366	0.087	6.63	0.32
3.54(2)	541.970	0.310	7.57	0.85	713.801	0.073	6.31	0.28	983.282	0.093	6.70	0.36
4.23(2)	543.472	0.214	8.15	0.59	713.601	0.062	5.91	0.25	986.009	0.073	6.82	0.25
4.54(2)	544.298	0.219	8.51	0.60	713.656	0.067	6.22	0.25	987.157	0.074	6.77	0.30
5.11(2)	545.183	0.225	9.84	0.62	713.489	0.072	6.13	0.29	989.257	0.082	7.92	0.31
5.42(2)	546.145	0.191	9.58	0.58	713.619	0.075	7.43	0.31	990.642	0.079	8.16	0.30
6.21(2)	547.739	0.164	11.22	0.66	713.553	0.070	7.13	0.28	994.007	0.069	8.49	0.26
6.95(2)	549.219	0.172	13.76	0.70	713.624	0.075	7.54	0.30	996.320	0.069	8.82	0.25
7.29(2)	549.756	0.156	14.27	0.63	713.717	0.066	7.04	0.27	997.816	0.066	9.29	0.23
7.86(2)	550.956	0.140	12.58	0.57	713.948	0.068	7.37	0.28	999.780	0.070	10.43	0.23
8.33(2)	552.085	0.107	10.83	0.43	713.968	0.054	6.46	0.22	1001.465	0.066	10.78	0.22
8.94(2)	553.566	0.107	11.25	0.43	714.416	0.063	6.08	0.25	1003.716	0.067	11.10	0.24
10.07(2)	553.936	0.217	12.91	0.88	710.799	0.134	8.98	0.54	1003.494	0.053	12.31	0.19

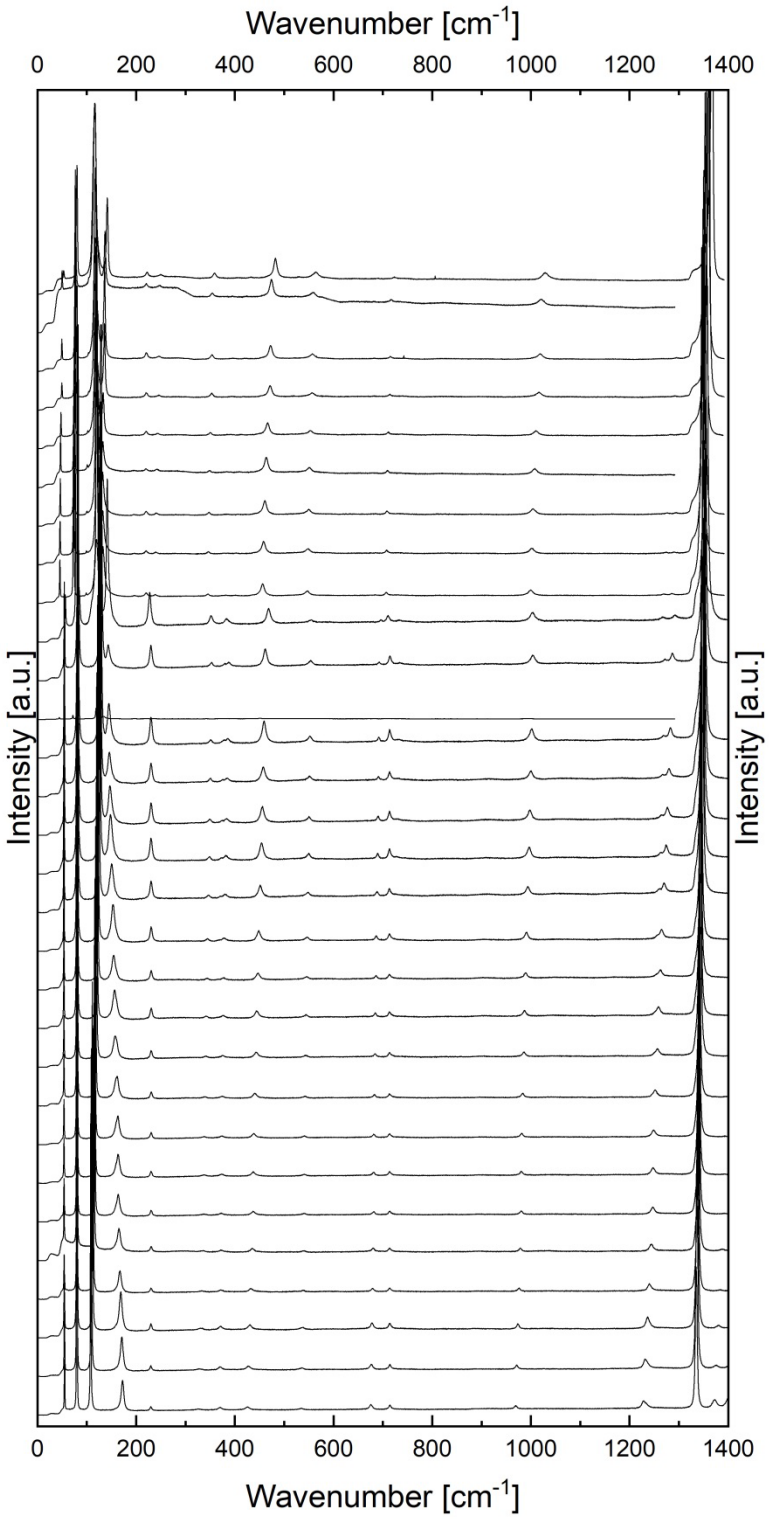

Waterfall plot of all Raman spectra measured from orientation “M1”.

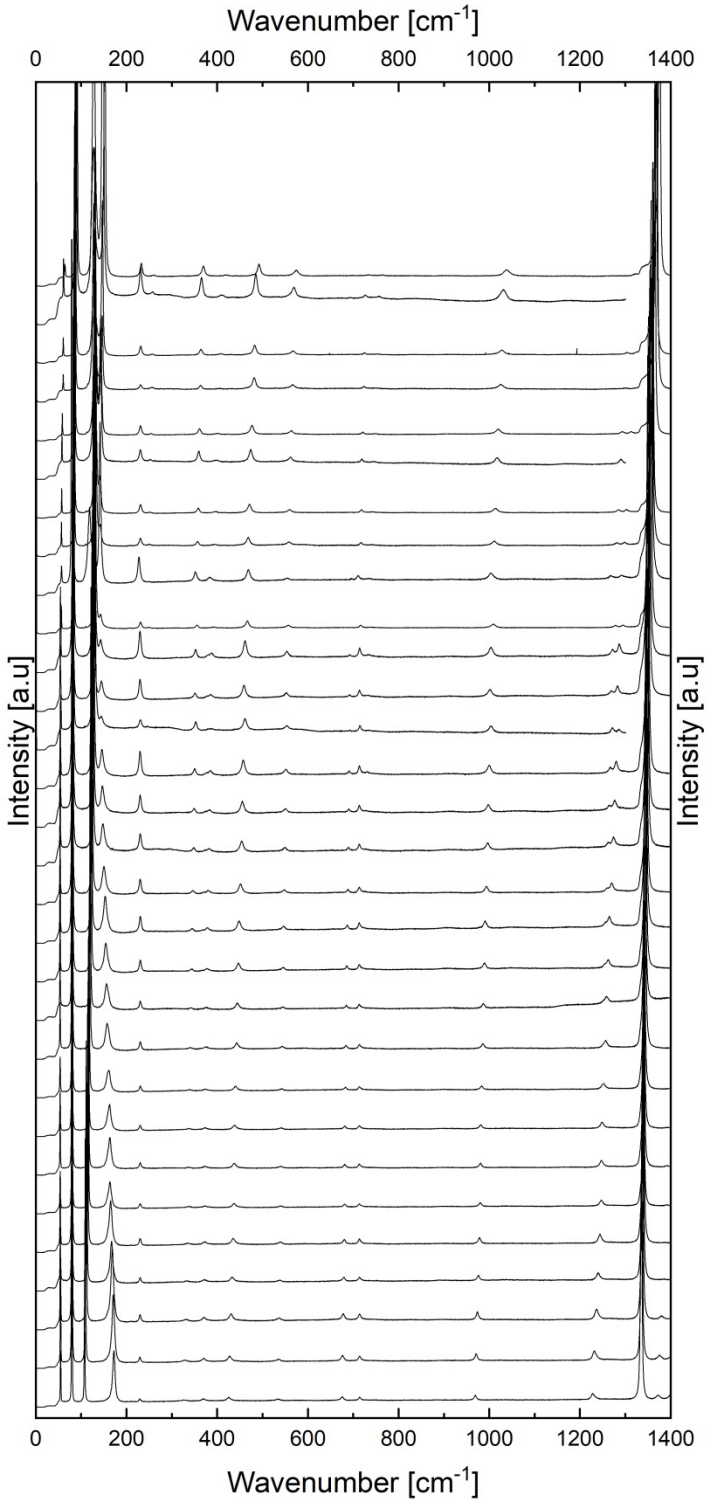

Waterfall plot of all Raman spectra measured from orientation “M2”.

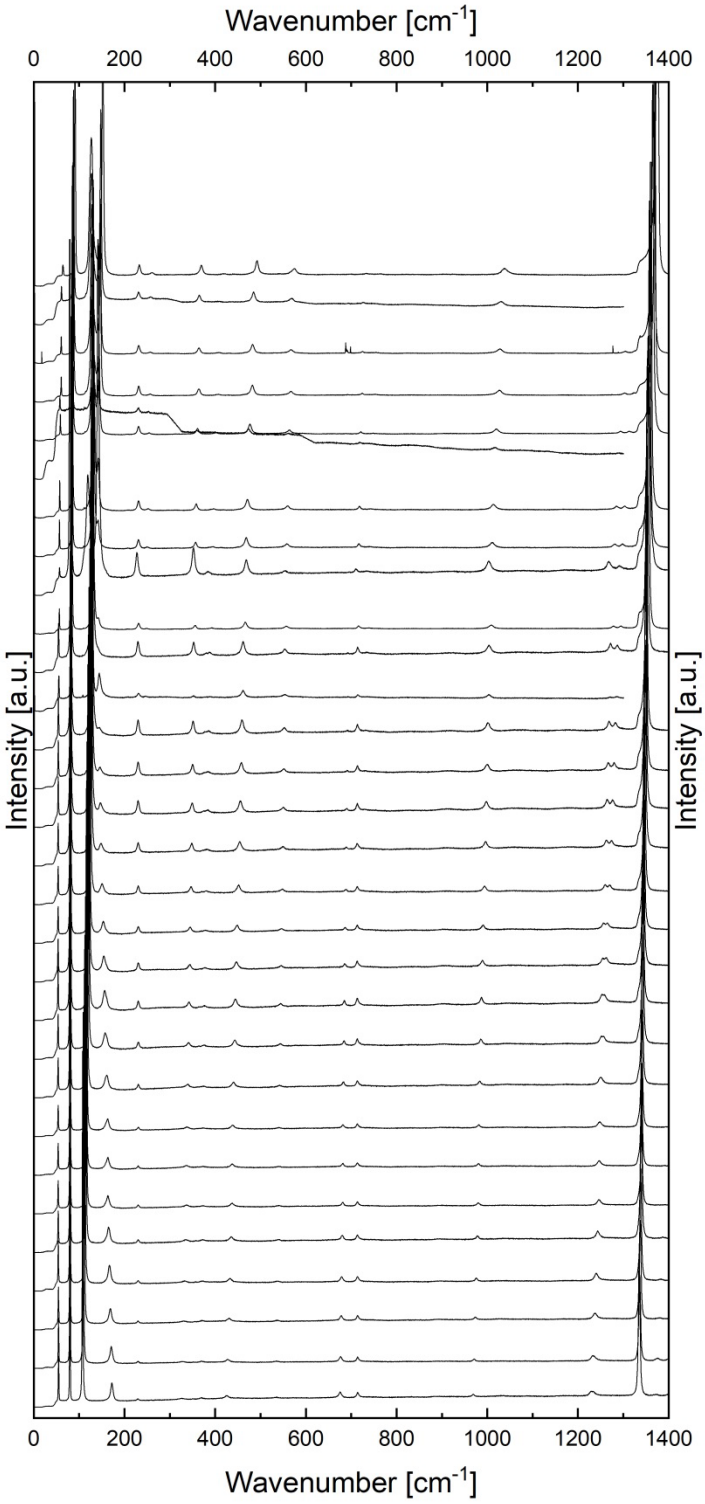

Waterfall plot of all Raman spectra measured from orientation “M3”.

ZUSAMMENFASSUNG

In dieser Arbeit wurde das neue Gasladesystem zum ersten Mal benutzt um ETH Diamantstempelzelle für Hochdruckexperimente mit Neon als Druckmedium zu füllen. Kleinere Anpassungen am Gasladesystem mussten durchgeführt werden, um dabei erfolgreich zu sein. In situ Hochdruck Röntgendiffraktometrie und Ramanspektroskopie wurde an synthetischen *α-PbAlBO$_4$* Einkristallen durchgeführt und Birch – Murnaghan Zustandsgleichungen dritter Ordnung wurden für die Messwerte berechnet. Für das Einheitszell-Volumen wurden V_0 = 322,38(6) Å³, K_0 = 77,5(1,2) GPa and K' = 7,3(4) and V_0 = 317,5(6) Å³, K_0 = 109(3) GPa and K' = 5 berechnet. Änderungen in den Positionen der Raman Banden deuten auf die Anwesenheit zweier sich überlagernder Kompressionsmechanismen hin. Der erste Mechanismus ist durch die Kompression des Hohlraumes, in welchem das einsame Elektronenpaar des Pb^{2+} Kations sitzt bestimmt, und der zweite Mechanismus ist durch die generelle Kompression der Struktur bestimmt.